Hochschule Karlsruhe – Technik und Wirtschaft

Fakultät für Maschinenbau und Mechatronik

Study of Transient Heat Transport Mechanisms in Superfluid Helium Cooled Rutherford-Cables

Masterthesis (M.Sc.)

Nr.: 16/009

von

Jens Schundelmeier

geb. am 29.03.1988

in Offenburg

Matr. Nr.: 50699

Betreuer der Arbeit
Prof. Dr.-Ing. Jens Denecke

Dr. rer. nat. Torsten Koettig

Meyrin, April 2016 — November 2016

Erklärung

Ich versichere hiermit wahrheitsgemäß, die Abschlussarbeit selbstständig angefertigt, alle benutzten Hilfsmittel vollständig und genau angegeben und alles einzeln kenntlich gemacht zu haben, was aus Arbeiten anderer unverändert oder mit Abänderungen entnommen wurde.

Unterschrift

Meyrin, den 30.11.2016

Kurzfassung

Untersuchung zum transienten Wärmetransport in superfluidem Helium gekühlten Rutherford-Kabeln

Der Teilchenstrahl im LHC (Large Hadron Collider) wird durch den Einsatz von supraleitenden Magneten auf seiner Kreisbahn gehalten und fokussiert. Diese Magnete bestehen aus NbTi-Kabeln in einer Kupfermatrix, umwickelt mit einer Spezialisolation, damit suprafluides Helium zur Kühlung eindringen kann. Verlustmechanismen, wie z.B. ein zufälliges verlassen der Teilchen aus dem Teilchenstrahl führen zu einer Erwärmung der Magnete. Dadurch kann eine lokale Erwärmung die Magnete über die Sprungtemperatur des Supraleiters erwärmen (Engl. quench) und diese möglicherweise beschädigen.

Ein detailliertes Wissen über die Wärmetransportmechanismen in den supraleitenden Kabeln (Typ Rutherford) ist daher essenziell, um einen effektiven Betrieb des LHCs zu gewährleisten.

Innerhalb dieser Arbeit sind mit einer Probe der inneren Dipolkabel des LHCs Untersuchungen zum Wärmetransport durchgeführt und ausgewertet worden.

Der Versuchsaufbau besteht aus einem Kryostaten mit einer supraleitenden Spule, die an Verlustmechanismen (Zwischenstrangwiderstände) in der Probe ankoppelt und dadurch Wärme in der Probe erzeugt. Die Kabeltemperatur wird mittels Temperatursensoren in der Probe gemessen.

Die Ergebnisse der durchgeführten Versuche zeigen ein turbulentes Kühlverhalten des Heliums bei Heizleistungen < 1,8 mW/cm³. Ein laminares Kühlverhalten, typisch bei kleinen Temperaturgradienten, konnte nicht beobachtet werden. Bei größeren Heizleistungen steigt die Kabeltemperatur linear mit der Heizleistung bis ein dominieren weiterer Heliumkanäle erfolgt. Je nach Dynamik des Temperaturanstiegs werden diese Kanäle deaktiviert und dominieren dann das Kühlverhalten. Weitere Versuche mit einer gesteigerten Heizleistung des Experimentaufbaus könnten die gefundenen Beziehungen bestätigen.

Die Ergebnisse wurden innerhalb einer intensiven Literaturrecherche mit experimentellen Ergebnissen, sowie Simulationen weiterer Forschungsgruppen verglichen und eingeordnet.

Das effektivste Kühlverhalten zeigte sich bei einer Badtemperatur des Heliums von 2.0 K.

Abstract

Study of transient heat transport mechanisms in superfluid helium cooled Rutherford-cables

The Large Hadron Collider leverages superconducting magnets to focus the particle beam or keep it in its circular track. These superconducting magnets are composed of NbTi-cables with a special insulation that allows superfluid helium to enter and cool the superconducting cable. Loss mechanisms, e.g. continuous random loss of particles escaping the collimation system heating up the magnets. Hence, a local temperature increase can occur and lead to a quench of the magnets when the superconductor warms up above the critical temperature.

A detailed knowledge about the temperature increases in the superconducting cable (Rutherford type) ensures a secure operation of the LHC.

A sample of the Rutherford cable has been instrumented with temperature sensors. Experiments with this sample have been performed within this study to investigate the cooling performance of the helium in the cable due to heat deposition.

The experiment uses a superconducting coil, placed in a cryostat, to couple with the magnetic field loss mechanisms in the sample (interstrand resistance) and deposit heat.

The results of this experiment show a turbulent behavior below a heating power of 1.8 mW/cm^3. A laminar performance could not be observed. However, at the higher heating powers a linear relationship of the temperature increase and the deposited heat was found up to a certain point, till some of the helium channels get deactivated. Depending on the dynamics of the heating curve, these channels play a major role and are dominant for the cooling performance. Further experiments with higher heating powers are needed to investigate this relationship.

The results of the performed experiments have been compared with further outcomes of research groups after an intense literature research within this thesis.

The experiments showed the most effective cooling at a bath temperature of 2.0 K.

Nomenclature

Latin Symbols

E	eV	Energy
B_a	T	Magnetic flux density
r_d	m	Bending radius
T	K	Temperature
j_c	A/m^2	Current density
c	J/kg·K	Specific heat
p	Pa	Pressure
$\dot{q}$	mW/cm^3	Heating power
F	N	Superfluid mutual friction force
A	m^2	Area
m	-	Superfluid thermal expansion coefficient exponent
f^{-1}	$kW/m^5 \cdot K$	Superfluid thermal expansion coefficient
h	$W/m^2 \cdot K$	Heat transfer coefficient
d	m	Diameter

Greek Symbols

α	1/K	Coefficient of expansion
λ		Lambda point
ρ	kg/m^3	Density
v	m/s	Velocity
j	$kg/m^2 \cdot s$	Superfluid motion
∇		Nabla operator
Δ		Delta
τ	s	Time constant

Abbreviations

LHC	Large Hadron Collider
MB	Main dipole
CERN	European Organization for Nuclear Re-
ATLAS	A Toroidal LHC ApparatuS

CMS	Compact-Muon-Solenoid
LHCb	Large Hadron Collider beauty
ALICE	A Large Ion Collider Experiment
PSB	Proton Synchrotron Booster
LINAC	Linear Accelerator
AC	Alternating Current
DC	Direct Current
SC	Super Conductor
GM	Gorter-Mellink
HT	High Temperature

Table of figures

List of tables

Content

Preface

The theory of nature is a wide field that could be described as one of the biggest puzzles mankind has been trying to solve for centuries. The so called “standard model”, a theory that is capable of explaining particle interactions, follows the question of how the laws of nature influencing our environment. A big role in this model plays the famously known Higgs-Boson, which was predicted by the early 1960s. Nevertheless, the scientists Brout, Engler and Higgs who formulated the theory about the Higgs mechanism, also predicted that it was almost impossible confirm this elementary particle experimentally.

In Meyrin, Switzerland an international project took on the challenge of verifying this particle and further theories by creating the largest experimental facility ever built. Therefore, the European Organization for Nuclear Research (CERN) planned the Large-Hadron-Collider (LHC) and started the construction in 1998. Involving around 10 000 international scientists and engineers helped the project to succeed by bringing all the knowledge together.

After finishing the construction of the LHC the experimental results led to a demand for higher luminosity and a deeper understanding of the operating principles within the accelerator complex and the detectors. This work is taking part in this learning process by investigating in a detailed way the cooling performance in the cable stacks of the superconducting magnets, which are used in the LHC to guide the particle beam.

In 2012 the Higgs-Boson was discovered, a huge success for CERN was done by evidence. Peter Higgs and Francois Englert were honored with the Nobel Prize in 2013 after the confirmation was brought for their theory of the origin of the mass of subatomic particles. The standard model of physics is now fully validated and the main experiment at CERN tries to look beyond this model and find new particles. [1]

Introduction

1.1 CERN and its accelerator complex

The idea of a European collaboration in the field of science became reality, when the European Council for Nuclear Research (CERN) was established close to Geneva at the Franco-Swiss-border in 1954. Since 2016, CERN has 22 member states and is an excellent example of how to bring nations together through science. The motivation behind this international project is to follow the fundamental questions of particle physics, e.g. what are the elementary particles, which forces are acting between them and what is the origin of mass?

CERN presented great achievements as an outcome of this mutual project in the past. To name some of the milestones: the discovery of the W and Z bosons, the invention of the World Wide Web and the experimental proof of the Higgs-Boson.

A large complex of particle accelerators is based underground at CERN to generate collisions between protons or heavy ions as given in figure 1. The most famous of those accelerators is the Large Hadron collider (LHC) located 100 m below the surface in the former tunnel of the Large Electron-Positron collider (LEP). The LHC measures a circumference of ~27 km and has four large detectors named ATLAS, CMS, LHCb and ALICE. The detectors at the collision points are triggered among others by a Muon detection to identify interactions. The measurement data of this events contain e.g. the charge of the particles as well as the momentum. Up to 600 million [2] of particle collisions happen in the LHC per second and create a huge amount of data, which is evaluated by the help of a worldwide network of computers.

To reach a velocity close to the speed of light in the LHC, an upstream chain of accelerators to the LHC has to be implemented. In proton operation, the orbiting electrons are stripped off from hydrogen atoms. These protons are injected in the Proton Synchrotron Booster (PSB) via a linear accelerator (Linac2). The PSB feeds the Proton Synchrotron (PS) and the particles reach an energy of 25 GeV. After the acceleration in the PS the Super Proton Synchrotron (SPS) accelerates the protons to a higher energy and feeds then the LHC where a final energy of 7 TeV is reached.

The acceleration of the particles in synchrotron accelerators is achieved by radio frequency cavities placed in the orbit of the named accelerators. The cavities separate the particles in bunches and generate signals that increase the particle velocity. [1]

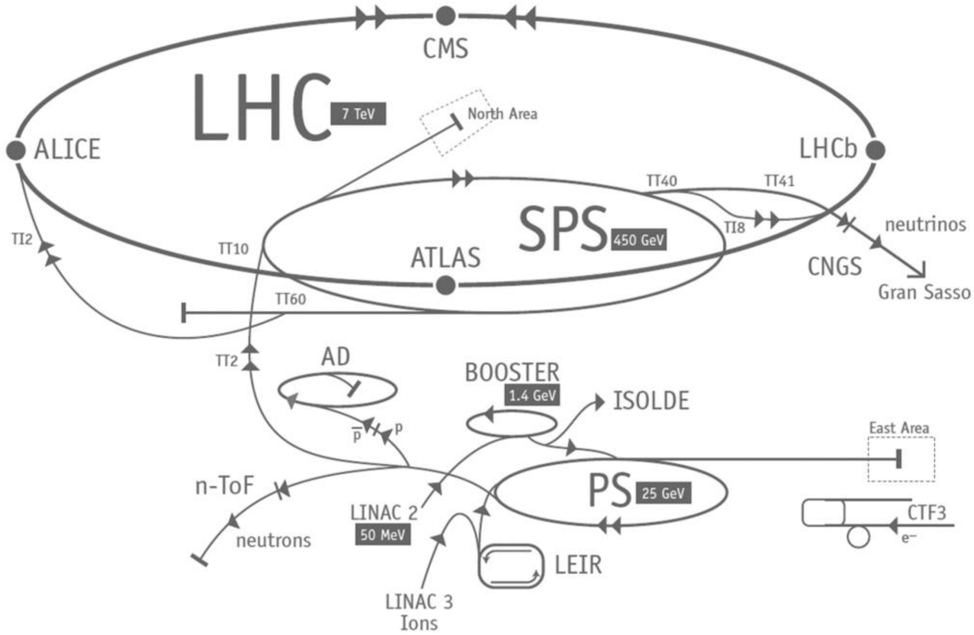

Figure 1: Scheme of CERN's accelerator complex and the provided nominal energies **[1]**.

1.2 Superconducting accelerator magnets in the LHC

Various magnets are produced by using normal conductors with iron and copper windings to create a magnetic field. However, the field strength of this type of magnets is limited due to the saturation of the used materials or enormous heat loads in DC operation. Superconductivity was discovered in the early 20th century and can be used to reach a much higher magnetic field than by normal conducting DC magnets, although there are only a few superconducting materials that can be used with a high magnetic field and a high current density.

The collision energy is a significant parameter of a synchrotron accelerator limited by the magnetic field of the bending magnets and their respective orbit radius. The collision energy can be calculated in TeV by the help of equation (1) where B_a is the magnetic field density in T and r_d is the bending radius of the dipole magnets in km.

$$\boldsymbol{E = 0.3 \cdot B_a \cdot r_d} \qquad (1)$$

Therefore, the demand for a superconductor with a high critical surface is given.

Niobium-titanium (NbTi) is the most common superconductor applied in accelerator magnets. It’s a well-studied material, but to realize even stronger magnets Niobium-Tin (Nb_3-Sn) is foreseen.

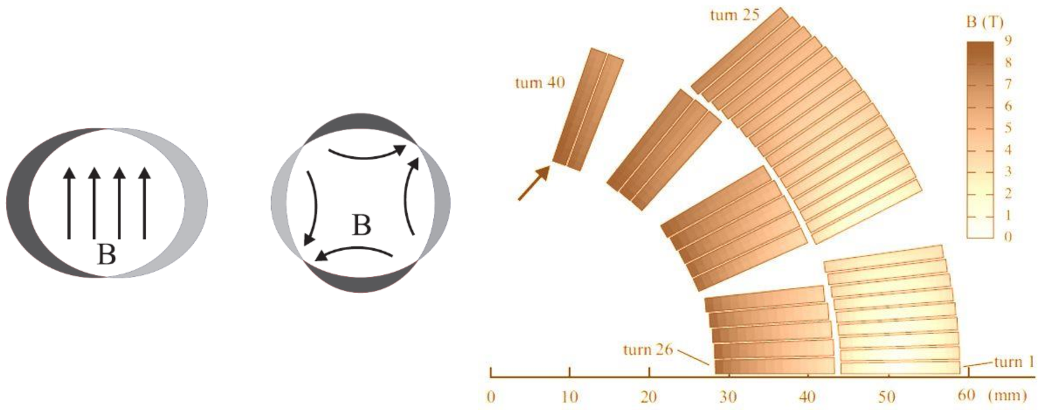

Figure 2: left: Current distribution for generating a pure dipole and quadrupole magnetic field. The arrows show the magnetic field direction with uniform current density in one direction in the light grey area and in the opposite direction in the dark area. Right: The magnetic field in the cables of one quadrant of an LHC dipole magnet with a central field of 8.33 T. The winding is divided in two layers consisting of two different cables, from **[3]**.

The usage of Nb_3-Sn in accelerator magnets is quite a promising technology, but challenging in its mechanical behavior, since it has to be heat treated to become superconductive and gets brittle after this process [4].

To operate particle beams in the dimensions of the LHC sophisticated systems of magnets are needed. The installed dipole magnets in the LHC can be considered as slow ramping magnets as they raise their field from 0.54 T injection energy to 8.33 T nominal field power within 1200 s. Dipoles bend the beam and keep it in its circular track in the LHC, but there are also quadrupoles positioned to focus and defocus the beam. A large number of higher order pole magnets are furthermore placed to correct the field distortion and chromaticity. The field is controlled within the magnets by the current and the turns of cables and the homogeneity of the field is optimized with wedges between the cable stacks. The ideal current distribution in a dipole and quadrupole is given in a cross section in figure 2.

The magnets in the main dipoles in the LHC consist of 25 turns LHC cable type 2 in the outer layer and 15 turns LHC cable type 1 in the inner layer. The highest magnetic field can be found in turn 40 of the inner cable.

The magnetic field distribution in the cross section can be described as in-homogeneous field as given in figure 2.

This magnetic field is obtained by using NbTi superconductors at a temperature of 1.9 K. That temperature is required to get below the critical temperature of the NbTi superconductor and provide a sufficient temperature margin for heat transfer across the electrical insulation. [5]

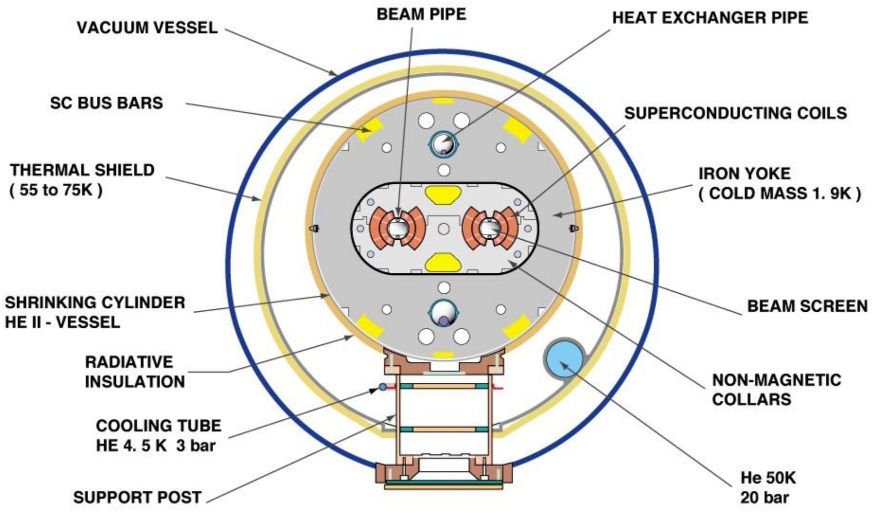

Figure 3: Cross-section of a main dipole bending magnet in the LHC **[6]**.

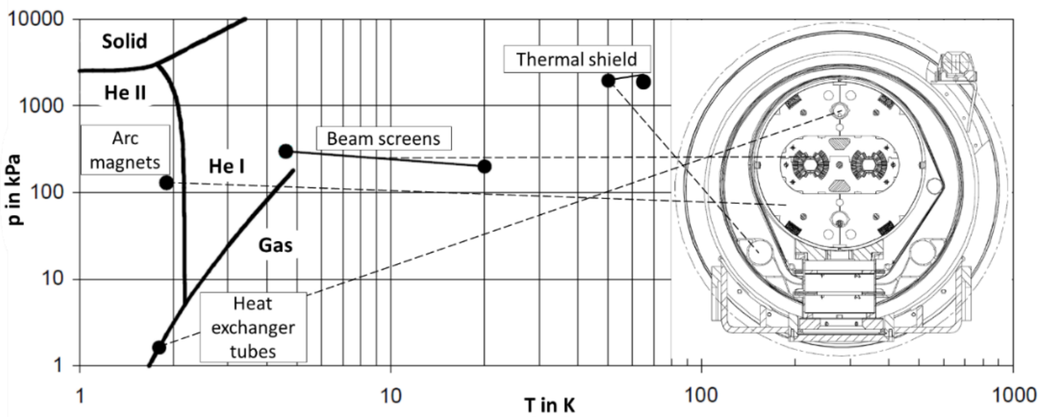

Figure 4: Operating conditions of the different cooling circuits in the LHC main dipole, re-drawn from **[5]**.

Figure 3 and figure 4 show a cross section of a LHC main dipole magnet including the temperature levels with a thermal shield at 55 K to 75 K and the magnet cold mass at 1.9 K. The heat exchanger pipe is filled with superfluid helium under saturation conditions to extract the heat from the magnets, whereas the cold mass and the superconducting coils are filled with pressurized superfluid helium, as it is illustrated in figure 4.

The iron yoke shields the exterior against the inner strong magnetic field. The nonmagnetic collars, which surround the superconducting coils, hold them in place against the strong magnetic forces during operation, pre-stress them and define their geometry. Surrounding the cold mass a vacuum tube provides the insulation vacuum and a multilayer superinsulation reduces the heat transfer by radiation. The beam itself is orbiting in an insulated bore tube under beam vacuum ($1.3 \cdot 10^{-7}$ Pa) to minimize collisions with residual gas molecules. Inside the bore, a beam screen made of copper coated austenitic stainless steel is located to reduce the amount of image currents in the magnet coils.

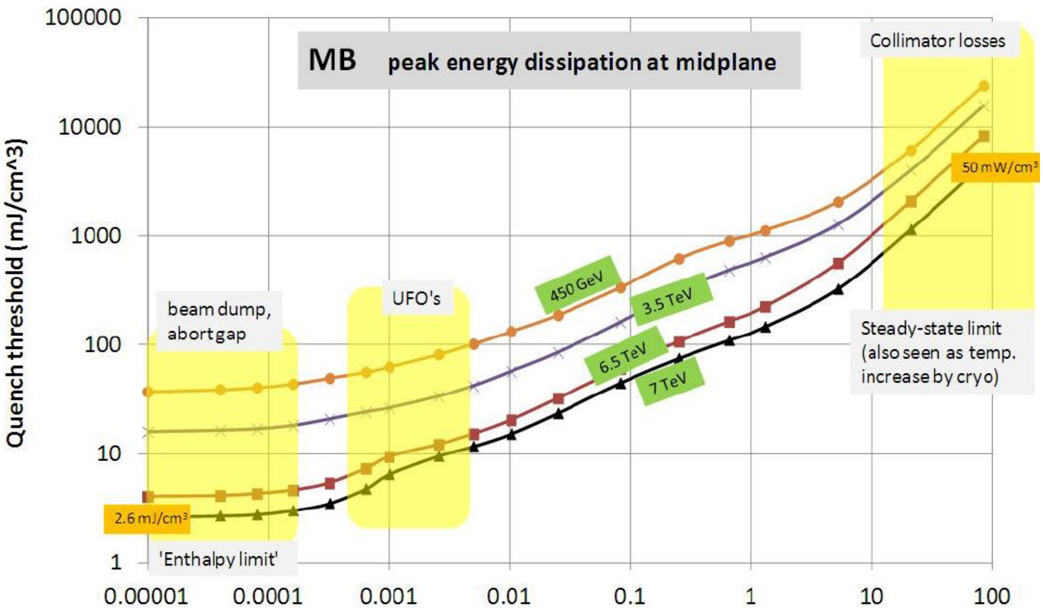

Figure 5: Calculated quench threshold for the main dipole, assuming maximum heat dissipation in the midplane of the magnet, reprinted from **[4].** The graph shows various transient phenomena that can cause quenches in the magnets. Further details can be found in **[4]**.

There are several transient beam induced heat loads that are occurring due to operation in the dipoles, like resistive dissipation in the resistive walls, nuclear inelastic beam-gas scattering, continuous random loss of particles escaping the collimation system and losses of secondary particles. The stated beam induced heat loads sum up to ~ 100 $mW \cdot m^{-1}$, whereas the beam gas scattering shows the highest contribution. [5]

During the operation of the LHC uncontrolled transitions from the superconducting state to the normal conducting state, named quench, can occur locally. In this case the temperature changes above the critical temperature of the superconductor for a given transport current and magnetic field value. Knowing the transient cooling performance of the Rutherford cables in the superconducting coils of the magnets is therefore essential for the operation of the LHC.

1.3 Scope of study

In order to gain a deeper understanding of the heat deposit in the magnets this work focuses on the investigation of the thermal phenomena that are occurring during beam operation in the cable. As stated in section 1.2 the different heat loads influence the helium temperature in the main dipoles. Therefore, a significant aspect for the operation of the magnets is the transient temperature rise in the helium bath and in the cable to perform particle accelerators at maximum possible beam energy and luminosity.

This thesis makes use of an experimental set-up, which allows to measure the temperature rise in a sample of a Rutherford-cable-stack cooled with superfluid helium. The dynamics of the presented set-up could also enable to take a look at transient mechanisms. Two Cernox®-temperature-sensors are positioned in the center of the cable and one is placed in the He bath to determine the temperature difference between the He bath and the cable, while the sample is subjected to a certain heat load.

Previous experiments about this topic were performed in a single strand by A.K. Gosh et al. [7] and in a cable by P.P. Granieri et al. [8] and C. Meuris et al. [9]. However, the named authors used a resistive cable mock-up to deposit heat via Joule-heating in the mock-up cable. The novel method to deposit heat in the used superconducting cable is realized by an outer AC electromagnetic field, which was firstly presented by T. Winkler [10] and further developed during this thesis. The herein presented system takes advantage by using an original superconducting cable sample. The results of this investigation provide the base for further simulations of the cooling scheme of the LHC and its upgrades.

Theoretical background

This chapter will provide an introduction to the used superconducting technology cable design and cooling scheme that are needed to understand the experimental work described in the following chapters.

2.1 Superconductivity and superconducting cables

Superconductivity was discovered first in mercury in 1911 [11]. A superconductor is mainly defined by its zero-electrical resistance below the critical surface. The critical surface is described with the critical temperature T_c, the magnetic field H_c and the current density j_c as shown in figure 6. Superconductors (SC) are separated in type I and type II SC. Super conductors type I are typically pure elements (e.g. Mercury) and show a sharp transition to the zero-resistance state. SC type I have the property of excluding magnetic fields from the interior of the superconductor (Meissner effect). Super conductors type II are made mostly out of alloys and show a much higher critical surface. Therefore, SC type II could carry much higher current densities while remaining in the superconducting state. Super conductors type II have an intermediate state where they appear in a mixed state of normal and superconducting regions, the so-called Shubnikov phase. Due to their performance, typical materials for SC magnets are NbTi and Nb_3Sn enabling the operation at high magnetic fields by the application of high transport currents in magnet coils.

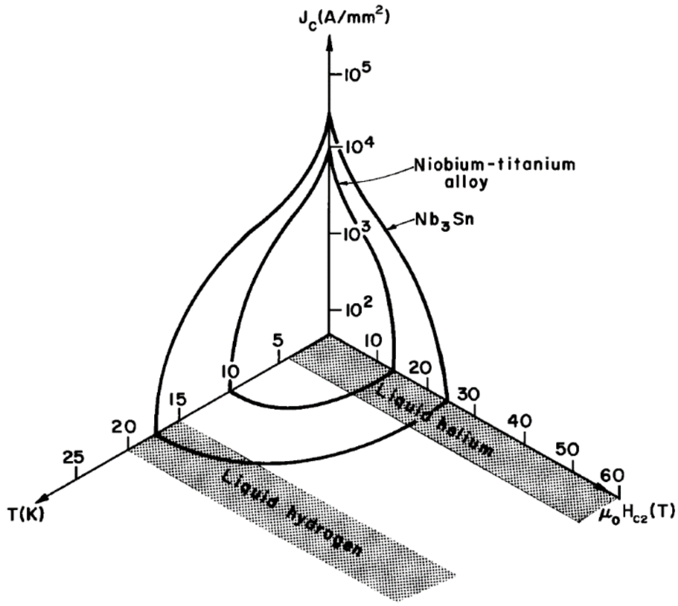

Figure 6: Graph of the upper critical field, temperature, and current density for commercial superconducting materials NbTi and Nb_3Sn **[11]**.

Since stability is a compulsory factor for the design of accelerator magnets, the cables for the magnets are not fabricated out of pure super conductors. Hence, typical SC-cables are made out of a well conducting matrix with embedded filaments of a SC material. As a usual material for the matrix, copper is used for the production of SC-cables to reduce Joule heating when the temperature in the SC gets beyond its critical temperature. An overheating of a SC-cables can also occur due to flux jumps provoked by a demagnetization. This effect is mainly reduced by a cable design with fine filaments of the SC material [4].

Various designs for SC cables exist on the market (e.g. Rope-, Braid- and Nuclotron type). In accelerator magnets, the most common used cable design is the one of the Rutherford type. It shows its advantages in a flat geometry which allows a good stacking and provides therefore high currents in the magnet structure. The magnets of the main dipoles in the LHC consist of a cable design with 28 strands in the inner coil. The thesis focuses on this specific geometry. In figure 7 the cable of a MB is illustrated and specifies its insulation scheme. The electrical insulation of the cable is made of a multiple machine wrapped Kapton® tape to insulate single cables within a stack from each other and allows the helium to enter to the strands of each cable. The primary insulation layer is made of two overlapping Kapton® 200 HN (50 µm, 11 mm) tapes with 50 % overlapping, while the secondary wrapping is applied on the outside with Kapton® 270 LCI-1 (67 µm, 9 mm). As investigated by C. Meuris [9], the Kapton® insulation is a dominant factor for the helium volume which cools the cable. The cable stacks of the LHC are pre-stressed and therefore the Kapton® is pressed in the cable voids of the broad plane of the Rutherford cable stack (see figure 8).

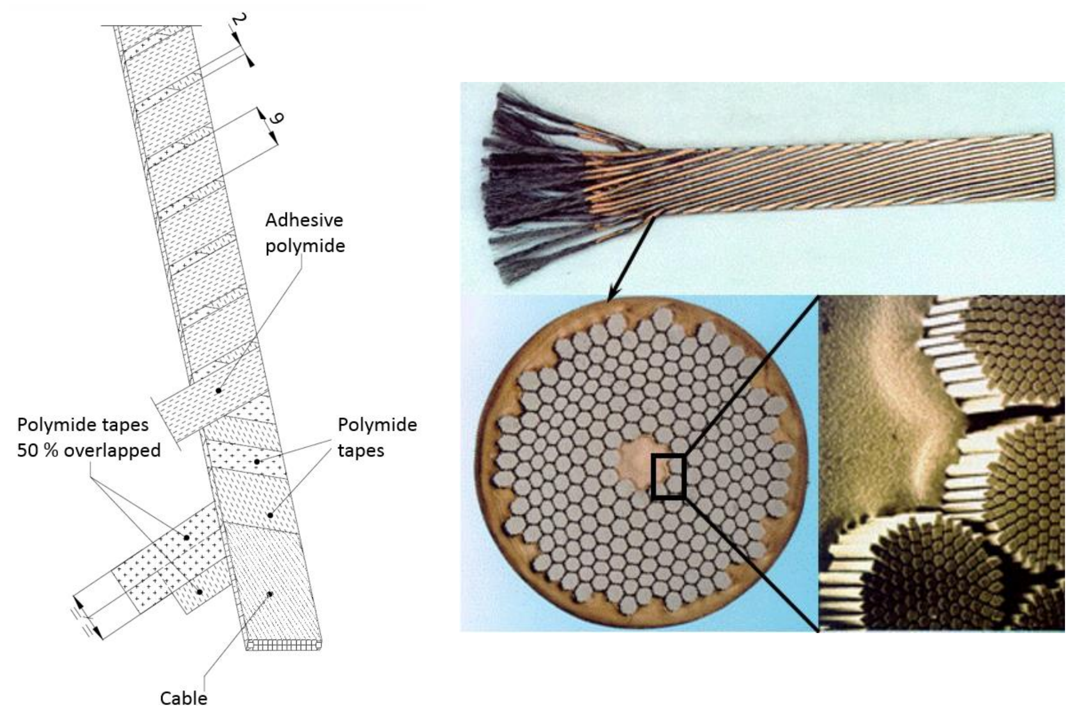

Figure 7: Left: Schematics of the insulation wrapping of 3 partially overlapping Kapton® tapes around the cable used in LHC dipole magnets, redrawn from **[5]**; Right: Rutherford cable partly without copper matrix, the lower pictures show a cross-section of a strand with about 8900 filaments. Filament bundles are stacked in a hexagonal structure as visible in the enlarged section. Rearranged from **[12]**.

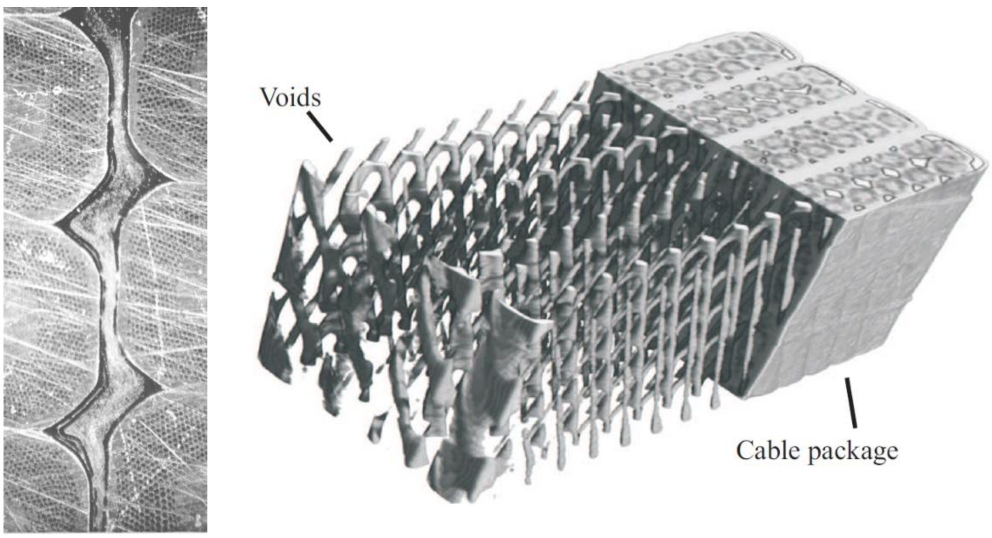

Figure 8: Left: Kapton® insulation has moved into voids within the cable stack after applying a mechanical compression of 60 MPa, reprinted from **[9]**. Right: 3D image of a stack of four LHC 01 cables. On the left side, only the cable voids are shown. On the right the cross-section of the cable package is visible, reprinted from **[3]**.

2.2 Liquid ^{4}He

Helium is an exceptional fluid due to its behavior and properties. It appears in two different liquid phases, the He I, also named normal fluid, and the He II, usually called superfluid. These two phases are separated by a second order phase transition, which means that there is no latent heat needed to convert He I into He II. The so-called lambda line, which starts at saturation condition at 2.1768 K separates these two phases. Figure 9 illustrates a pressure-temperature diagram and outlines the states of helium under different conditions. A special property of helium is that, due to its two liquid phases, it has no triple point. He II behaves nearly like an ideal thermodynamic fluid and attain consequently the name superfluid helium. He I behaves completely different from the superfluid helium and approximates common liquids from its behaviors. A solid state of helium can be only reached by an external moderately high pressure.

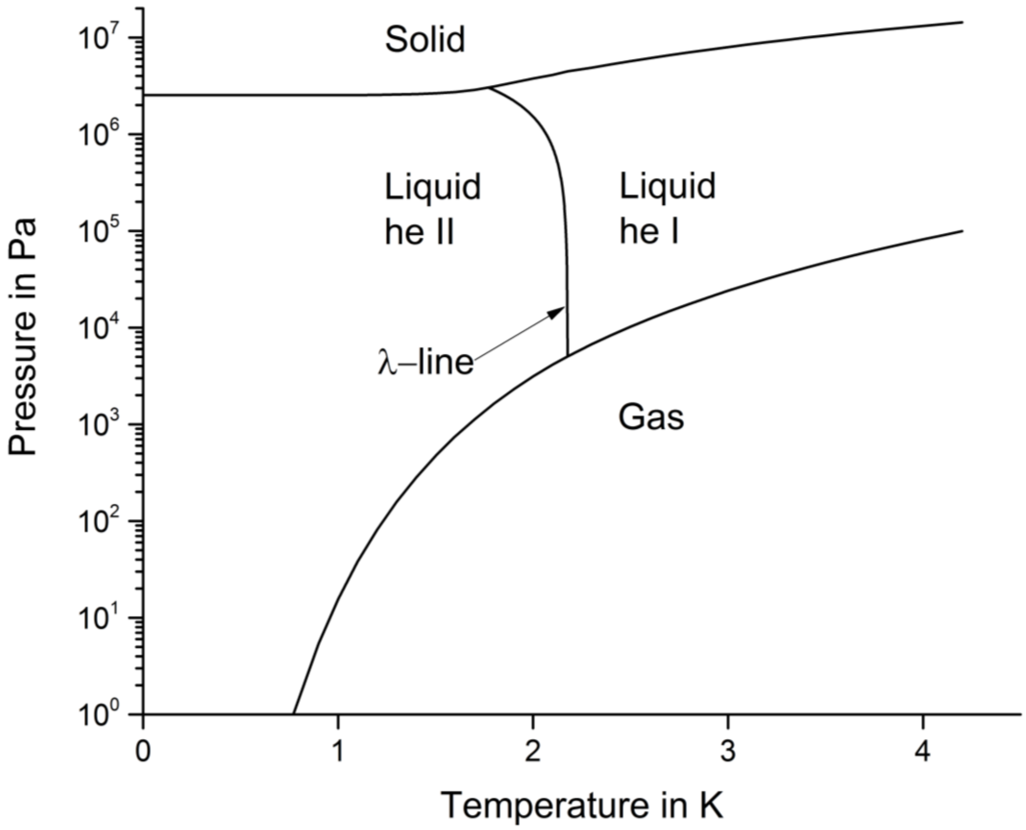

Figure 9: p-T Diagram of ^{4}He, data determined with HePack **[13]**.

2.2.1 Thermodynamic properties

The atoms in liquid helium are not closely packed and show a relatively large distance to each other [11]. Inferred to this, the density of He I is quite low with 125 kg/m^3 at atmospheric pressure which is only ~13 % of the density of water. The density of liquid helium increases towards lower temperatures and reaches after the phase transition to a constant value around 145 kg/m^3.

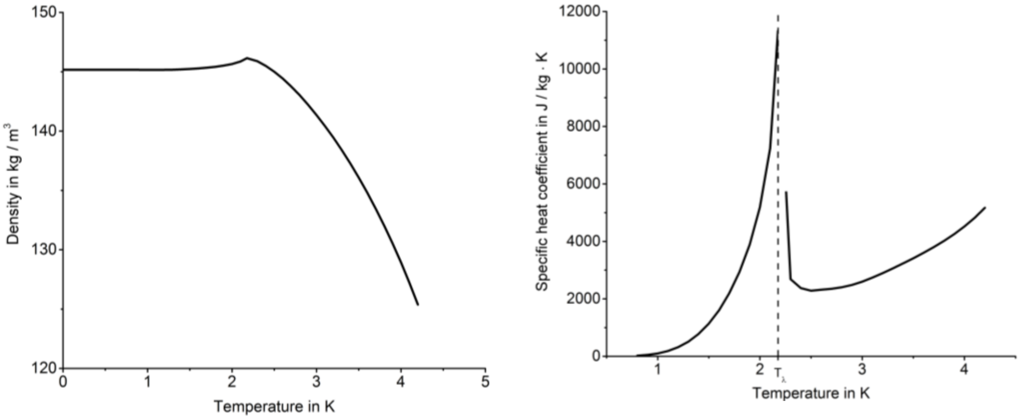

Figure 10: Left, density of ^{4}He vs. temperature. Right: Specific heat coefficient of ^{4}He vs. temperature, data determined with HePack **[13]**.

The specific heat can be determined by measuring the temperature rise when heat is supplied to a known mass of liquid insulated from its environment. The specific heat for liquid helium has an anomalous rapid rise at the lambda point and a discontinuous fall above that temperature. Figure 10 shows the specific heat at a constant saturated vapor pressure c_{sat}, which differs below 2.5 K less than 1 % from the specific heat under the constant pressure [14]. The relation between c_{sat} and c_p is given in equation (2).

$$c_{sat} = c_p - T \cdot V \cdot \alpha \cdot \left(\frac{dp}{dT}\right) \quad (2)$$

Where α is the coefficient of expansion and (dp/dT) the slope of the vapor pressure curve.

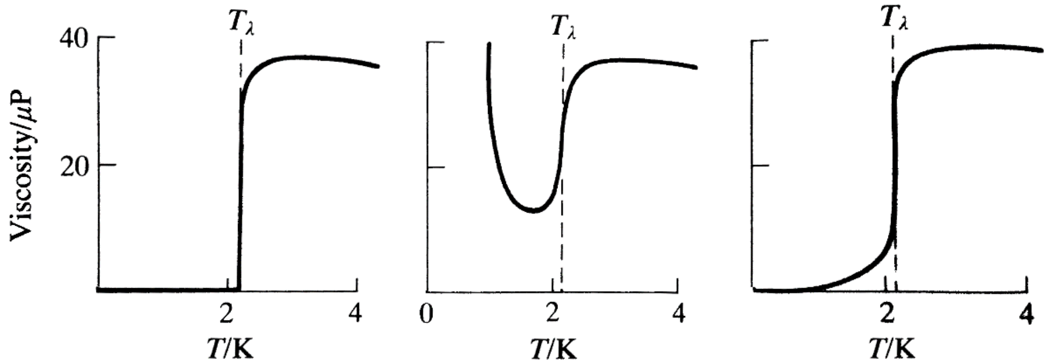

Figure 11: Schematic illustration of the viscosity of liquid ^4He measured by different methods. From left to right: by a Poisseuille flow method; in a rotation viscometer; in an oscillating disc viscometer, reprinted from **[15]**.

The viscosity of liquid helium can be measured by different principles and show according to the applied method a different shape of the measurement curve below the lambda-transition-temperature.

In compliance with the two-fluid model, further explained in section 2.2.2, the viscosity of helium II in fine capillaries drops down to zero and shows one of the most characteristic values of He II, the superfluidity. In contrary to that, a measurement with a rotating disc is more dominated by the normal fluid component and the viscosity decreases significantly below T_{lambda} and rises up after a minimum around 1.8 K. A similar behavior to the rotating disc experiment is expected with oscillating discs, but there has to be mentioned that the damping of helium II is a function of the amplitude of the oscillating discs.

2.2.2 Two fluid model

The two-fluid model considers helium II as a mixture of two fluids intermingling with each other. The fluid density is a sum of the normal fluid ρ_n and the superfluid ρ_s component.

$$\rho = \rho_n + \rho_s \quad (3)$$

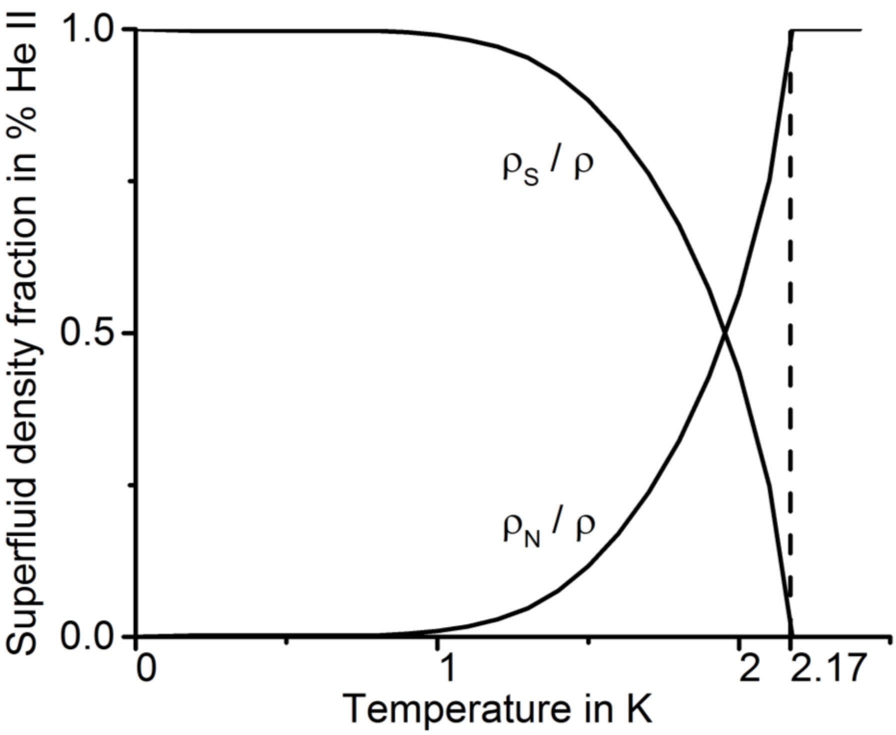

Figure 12: Superfluid density fraction of ^4He, data determined with HePack **[13]**.

Figure 12 illustrates the ratio of the normal and the superfluid component in helium II and its temperature dependency within the two-fluid model.

The model characterizes furthermore the superfluid component with zero entropy and no viscosity wherever it flows. If motion is involved the superfluid has a certain velocity. Hence, the momentum can be determined with equation (4).

$$\vec{J} = \rho_n \cdot \vec{v_n} + \rho_s \cdot \vec{v_s} \tag{4}$$

The motion of superfluid helium shows stable flow patterns for small v_s and v_n and satisfies the Laplace equation. Thus, a pure potential flow exists for a constant density of the superfluid.

A single vortex is in the two-fluid model pictured as a circulation of the superfluid around a vortex axis of predominantly normal fluid component.

Table 1 gives a plain description of the relations within the two-fluid model.

Table 1: Parameters of the two-fluid model

Normal fluid	ρ_n	$\eta_n = \eta$	$S_n = S$	v_n
Superfluid	ρ_s	$\eta_s = 0$	$S_s = 0$	v_s

2.3 Heat transfer mechanisms in He II

The basic heat transport mechanisms are based on the two-fluid model. Following this, the superfluid component has zero entropy and the heat transport is accomplished purely by the motion of the normalfluid component.

$$\dot{Q} = \rho \cdot S \cdot T \cdot v_n \qquad (5)$$

If there is no net mass flow, the additional boundary conditions of equation (6) are given. The brackets in this term denote an average of the cross section perpendicular to the heat flow.

$$< \rho_n \cdot v_n + \rho_s \cdot v_s > = 0 \qquad (6)$$

At the surface of the heat source excitations are created in the He II, which leads physically to a flow away from the heat source of the normal fluid component while the superfluid goes in counter flow direction. An exceptional behavior of helium is the fact, that a temperature gradient causes a relatively large pressure gradient in the superfluid component (see equation (9)). The flow of the superfluid towards the heat source is balanced by the counter flow of the normal fluid. The heat transport mechanism of the counter flow is far more effective than only conduction in He II [16] and is dependent on the relative velocities of the two components. Therefore, an existence of a laminar regime for low velocities and a turbulent for the high velocities is known. The transition from the flow regimes from one to the other occur at critical heat fluxes $\dot{Q}_c$. Referred to this the effective thermal conductivity is a function of $\dot{Q}$ and the geometrical factors. The hydrodynamic equations for the two components can be formulated as a modification of the classical Navier-Stokes equation as followed [16]:

$$\rho_n \cdot \frac{\partial v_n}{\partial t} + \rho_n \cdot v_n \times \nabla v_n = -\frac{\rho_n}{\rho} \nabla p - \rho_S \cdot S \cdot \nabla T + \eta \nabla^2 v_n + F_{sn} \qquad (7)$$

$$\rho_s \cdot \frac{\partial v_s}{\partial t} + \rho_s \cdot v_s \times \nabla v_s = -\frac{\rho_s}{\rho} \nabla p + \rho_s \cdot S \cdot \nabla T - F_{sn} \qquad (8)$$

The superfluid component is marked in the previous equation with the indices s and the normal component with n. The diffusive term of the velocity in equation (7) appears only in the normal fluid component and is controlled by the viscosity. The mutual friction has to appear in equation (7) and (8) in opposite direction.

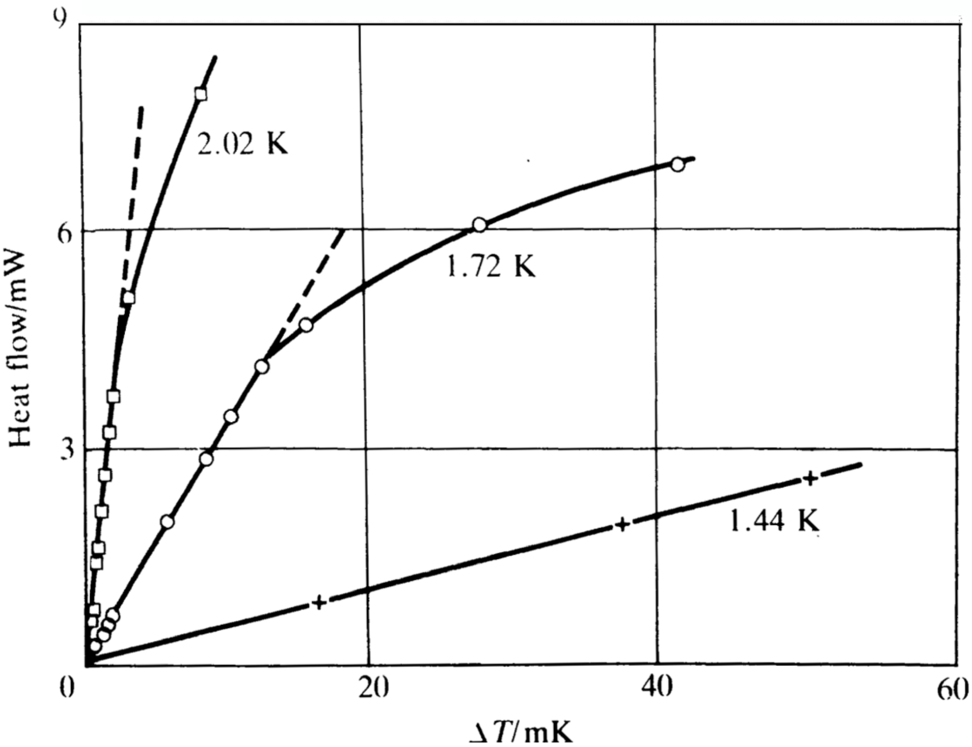

Figure 13: Heat flow through liquid helium in a slit of width 2.4 µm as a function of the temperature difference ΔT across the slit, reprinted from **[15]**.

2.3.1 Landau regime

Small thermal heat flows causing for relatively slow velocities v_n and v_s. The mutual friction and the acceleration terms play in the laminar regime a minor role and can be neglected. The second law of thermodynamics allows to formulate the London equation (9). [17]

$$\nabla p = \rho \cdot S \cdot \nabla T \qquad (9)$$

In addition, the Poisseuille equation can be applied for the normal fluid, as a laminar flow is caused due to the pressure gradient [16].

$$\nabla p = \eta \cdot \nabla^2 v_n \qquad (10)$$

The solution for a squared channel geometry with the hydraulic diameter d_h is [16]:

$$\nabla p = \frac{48 \cdot \eta \cdot v_n}{{d_h}^2} \qquad (11)$$

A combination of equation (5) and (11) gives the temperature gradient for the laminar regime.

$$\nabla T = \frac{12 \cdot \eta}{\rho^2 \cdot S^2 \cdot T \cdot h^2} \cdot Q \qquad (12)$$

Where h is the height of the channel. By the use of equation (12) and experimental determined values for the temperature rise and the controlled heat input the channel size can be calculated for the laminar regime. With the approach of equation (12) and the channel size further calculations for the critical heat flow can be made.

2.3.2 Gorter-Mellink regime

The turbulent regime is in contrary to the Landau regime dominated by the mutual friction term. The turbulent regime was further investigated by Gorter and Mellink [18] and they showed that thermal conduction and pressure gradients in superfluid helium are consistent with:

$$F_{sn} = A \cdot \rho_s \cdot \rho_n \, |v_s - v_n|^m \qquad (13)$$

Where A is the Gorter-Mellink constant and m in the exponent is an experimental determined factor equal to 3 [18]. Further investigations by van Sciver [11] have shown better achievements with the factor m=3.4. The acceleration term containing ∇p and the viscous term $\eta \cdot \nabla^2 v_n$ are negligibly due to a dominance of the mutual friction, therefore the thermal gradient can be calculated with the help of equation (14).

$$\nabla T = \frac{F_{sn}}{\rho_s \cdot S} \qquad (14)$$

To bring the thermal flow in relation to the thermal gradient equation (4), (5) and (13) have to be combined.

$$\nabla T = \frac{A \cdot \rho_n}{S} \cdot \left(\frac{Q}{\rho_s \cdot S \cdot T}\right)^m \qquad (15)$$

The effective thermal conductivity is in the turbulent regime independent of the channel size. Thus, a function of the superfluid thermal conductivity can be defined and is dependent on the temperature and the pressure. The influence of the pressure plays compared to the m-factor in the exponent a minor role in the order of magnitude of the superfluid thermal conductivity function.

$$f = \frac{A \cdot \rho_n}{S} \cdot \left(\frac{1}{\rho_s \cdot S \cdot T}\right)^m \qquad (16)$$

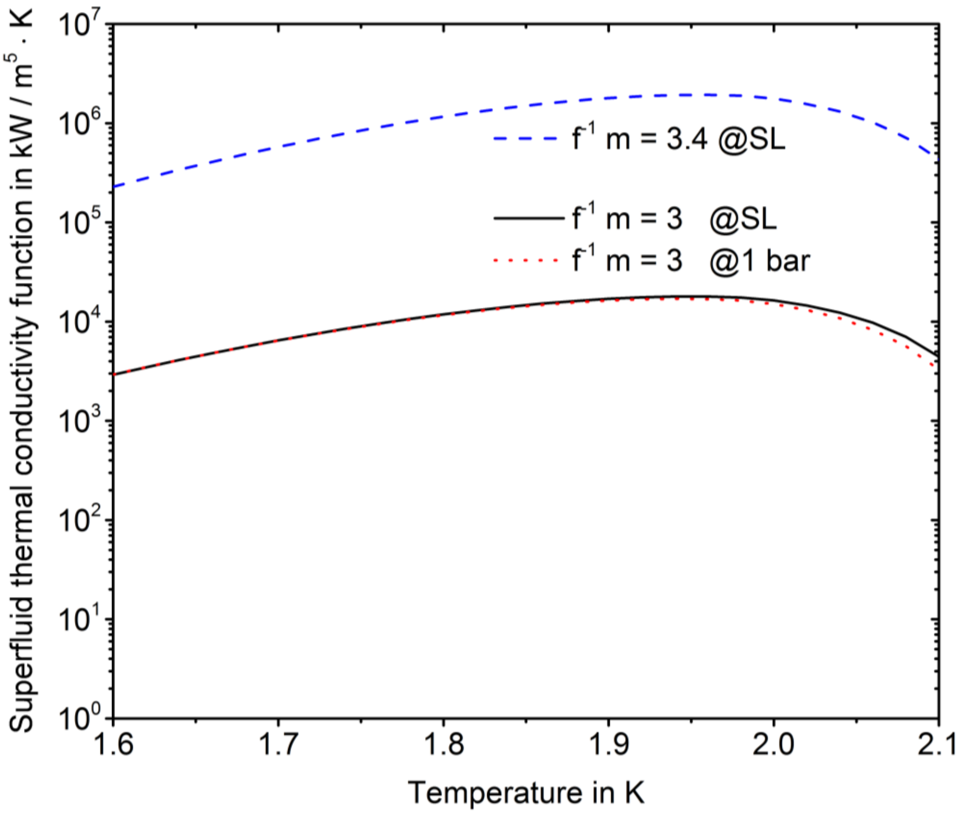

Figure 14: Variation of the f^{-1} function to a different m-exponent and pressure, SL indicates saturation conditions, data determined with HePack **[13]**.

Figure 14 highlights that a variation of the m-exponent results in a several orders of magnitude different f^{-1} function. The theoretical relation in the Gorter-Mellink regime between ΔT and Q is therefore highly dependent on this value.

2.3.3 Kapitza conductance at low temperatures

A thermal boundary resistance between a solid body and liquid helium was firstly observed by P.L. Kapitza in 1941 [11]. He performed an experiment to investigate the temperature gradient from copper to liquid helium II and detected a significant temperature difference at the interface (see figure 15, left). Two main theories have been established to describe this phenomenon, the acoustic mismatch theory by Khalatnikov and the theory of phonon radiation [11]. Whereas the acoustic mismatch theory is more appropriate for temperatures <1 K and the phonon radiation theory covers a more conservative consideration with too many energy transport mechanisms.

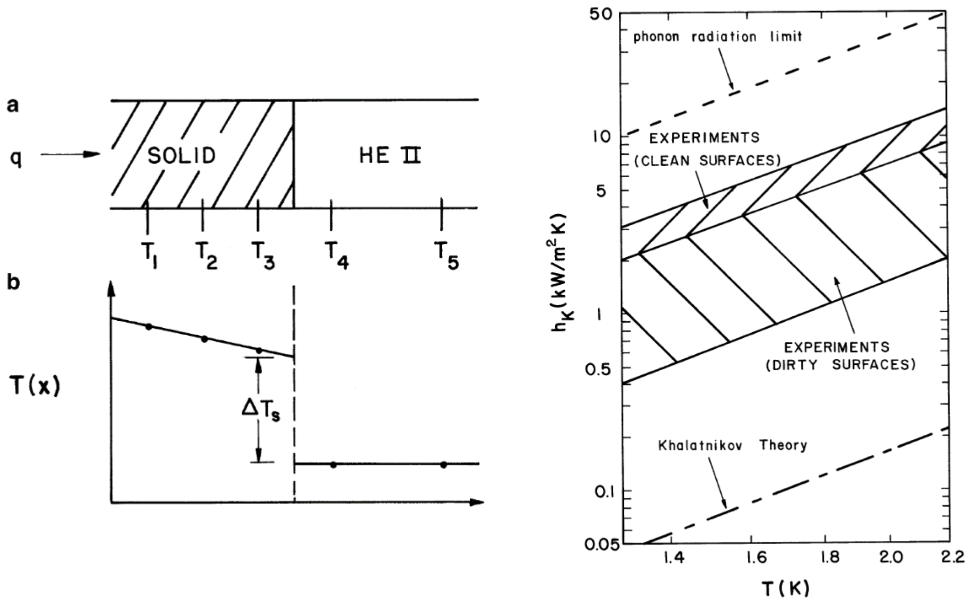

Figure 15: Left: Schematic of Kapitza conductance experiment: (a) temperature sensors located in the vicinity of a solid-He II interface and (b) temperature profile; Right: Experimental values for the Kapitza conductance of copper between 1.3 K and the lambda temperature, reprinted from **[11]**.

The Kapitza conductance is generally in a practical expression formulated:

$$h_k = \frac{q}{\Delta T_s} \qquad (17)$$

Among others, the Kapitza conductance depends on the temperature, the surface roughness and the shape of the solid. Hence, experimental data and the mentioned theories don't concur due to its complexity (see figure 15, right). The mechanism of Kapitza conductance dominates at low temperatures ($T<T_\lambda$) when no boiling occurs. The heat transfer coefficient of film boiling is 10-100 times smaller than the Kapitza conductance coefficient [11].

2.3.4 Intermediate thermal flux

The phase transition of liquid helium occurs at the critical heat flux q_C. In this state, no clear correlation to concepts of turbulence and quantized vortices seem to be appropriate [16]. An approach to calculate the critical velocity v_{SC} and q_C, where turbulences in the superfluid appear was presented by Alphen et al [19], but further experiments have shown different results [16]. When the velocity of the vortexes is higher than the critical value it results in a perturbation of the vortexes in the superfluid, thus a very low thermal conductivity can be observed.

2.3.5 Time dependent effects

The previous described mutual friction was reported to have a time dependent behavior [20], [21]. When a heat source is triggered in helium II it takes between 0.1 and 50 s to reach a steady state [16]. The quantity of the transient behavior can be described with an experimental parameter (see equation (18)). The experiment of Chase [21] investigated the transient behavior of helium II with different channel diameters and shapes. The results can be seen in figure 16.

$$\tau = a * Q^{-\frac{3}{2}} \qquad (18)$$

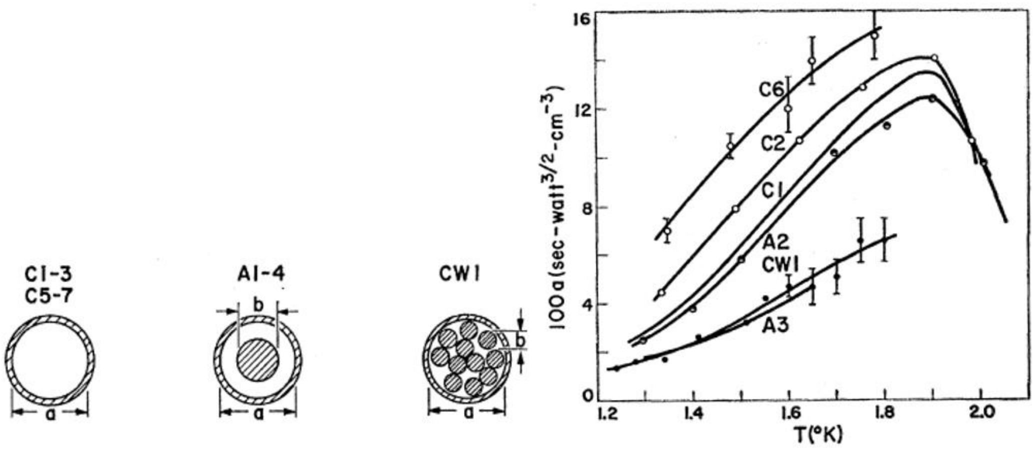

Figure 16: Temperature dependence of the quantity a in the relation tau=a*$Q^{-3/2}$, Channel diameter in mm: C1= 2.62 mm, C2=4.04 mm, C6=0.8mm, reprinted from **[21]**.

A bigger channel size shows from the results of Chase a higher time parameter, i.e. a longer time to reach steady state conditions for the mutual friction. For fine channels, the quantity varies in a negligible range.

Experimental work

The experimental set-up consists of a sophisticated cryogenic measurement system and a well-insulated cryostat. In the following paragraphs, different aspects are presented.

3.1 Set-up

The set-up can be simply structured for a better comprehension in the following sub-parts:

- Cryostat
- Temperature regulation
- Optional glass fiber epoxy pot
- Measurement instrumentation

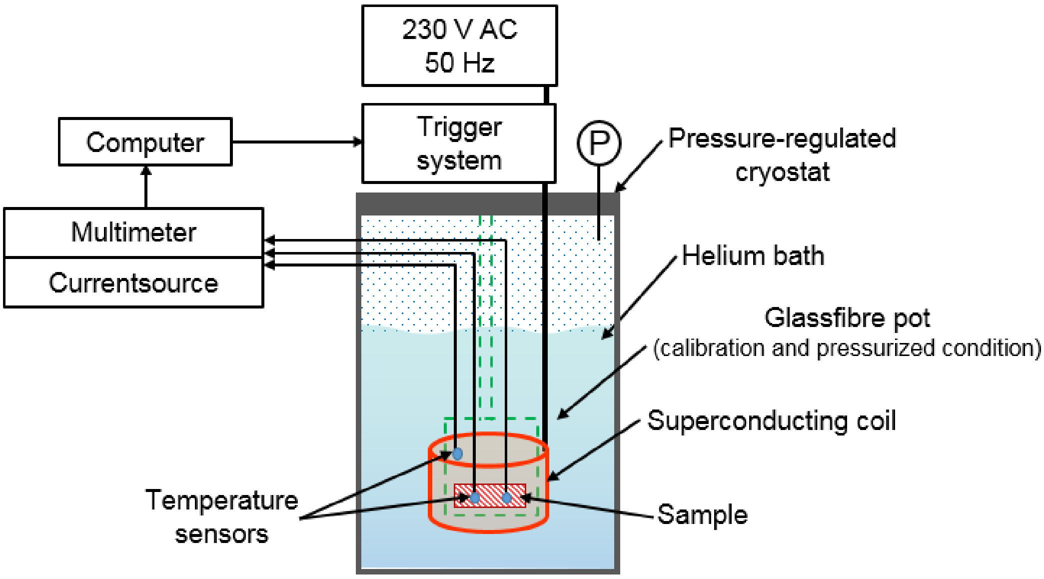

Figure 17: Schematic illustration of the measurement set-up.

3.1.1 Cryostat

A cryostat is a vessel to maintain low temperatures for cryogenic applications. The here utilized cryostat measures 2 m of height to obtain a relatively high level of liquid helium. The liquid helium evaporates due to the deposited heat during the experiment and a static height of the bath is essential to ensure pressurized helium conditions at the sample position, which is further explained in 4.4. The cryostat is equipped with thermal shields and a vacuum insulation to keep the temperature constant, even for liquid helium temperatures (<4.2 K).

Before every measurement campaign, a leak test is performed to guarantee a leak rate < 1 mbar/h in the cryostat. Influences of gas impurities are minimized by initial multiple purging of the system.

3.1.2 Temperature regulation

To achieve a stable operating temperature of 1.7 K, pumping is used to reduce the saturation pressure of the helium bath. A positive displacement lobe pump (Roots type) achieves in the with liquid filled cryostat steady conditions for pressures > 1000 Pa, also for the maximum induced heat in the sample. A pressure regulation through a control valve allows to achieve a stable saturated bath temperature. Thus, temperature is not controlled directly, but through the saturation pressure.

3.1.3 Optional glass fiber epoxy pot

A glass fiber reinforced epoxy pot can be placed surround the sample to allow a calorimetry of the deposited heat in the sample (see section 3.3) or to fill it with helium, pressurized with an outer helium source. The optional pot is essential for measurements close to the lambda-temperature, since a second order phase transition has to be investigated. The pot (see figure 18) is equipped with a special designed safety valve that can also be actuated externally to open the glass fiber pot to the outer bath of the cryostat. A cooling loop made out of copper on the top of the glass fiber pot is installed to exchange the heat between the pot and the outer bath.

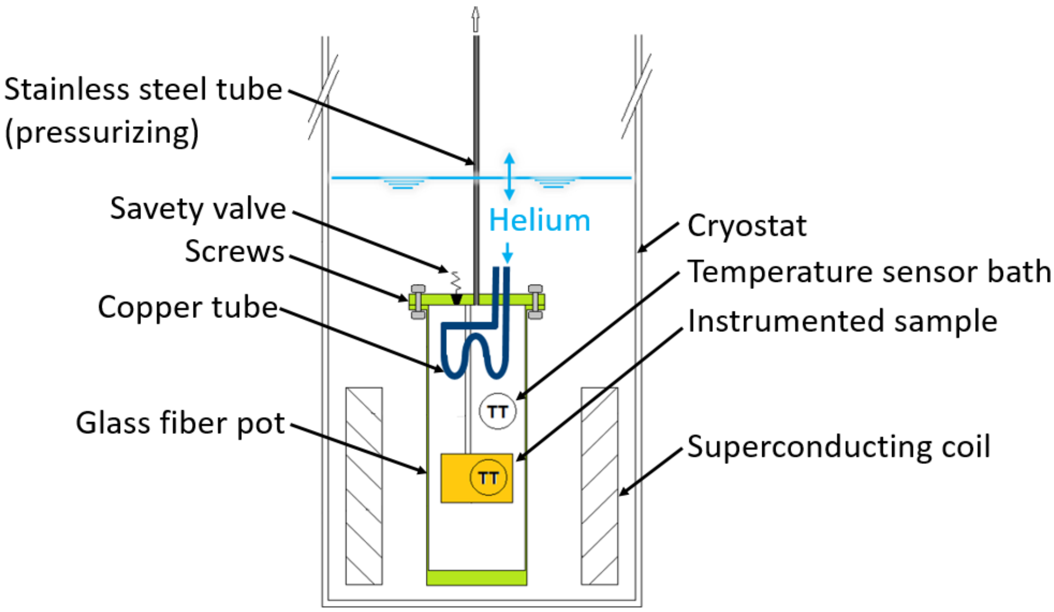

Figure 18: Schematic illustration of the optional glass fiber pot in the experimental setup.

3.1.4 Instrumentation and data acquisition

The sample itself is instrumented with two symmetrically placed temperature sensors (further described in section 3.2) to measure the sample temperature. Supplementally, a further temperature sensor is kept in the bath to measure its temperature. The temperature sensors are supplied with a current of 3 µA ±50 pA and calibrated via the mounted pressure sensor with 0.25 % accuracy of reading. The helium level is measured with a level gauge of 1800 mm length, which is made out of a porous metal that becomes superconducting in the liquid helium. The heat in the sample is provoked by the magnetic field of the super conducting coil, which couples on the interstrand resistance in the sample.

The installed measurement card allows to measure with a frequency of 20 Hz per channel. The sample is placed horizontally in the middle of a superconducting coil, which is triggered with 230 V AC and a power line frequency of 50 Hz to couple on the interstrand resistance in the sample and induce heating. The inductance of the magnet measures 0.5 H and creates a 4 T field at 400 A DC. A variation of power resistors (50, 125 and 250 Ohm) in series with the coil achieve a lower magnetic field strength. Optionally a pot designed out of glass fiber can be mounted in the cryostat. The glass fiber reinforced epoxy pot is leak tight and has a copper loop with the objective of exchanging the heat in the pot and the outer helium bath. Furthermore, the pot has a pipe connection to the outside and allows to control the pressure in the pot.

3.2 Sample preparation

The sample consists out of four machine wrapped Rutherford cables, following the same insulation scheme like the inner MB cable in the LHC. The first- and second wrap have 50 % overlap and consist of 50 µm thick Kapton® tape with 11 mm width. Thus, the insulation is simultaneously wrapped with a shift of half of the width to achieve the 50 % overlapping. The third layer is wrapped in the opposite direction and measures 69 µm thickness and 9 mm width with 2 mm spacing. The cables have a trapezoid shape due to the mechanical treatment. Therefore, the cables in the stack are stapled in opposite directions to equalize the height of the stack. The cables measure on the thin side a height of 1.736 mm and on the thick side 2.064 mm. Hence, an average height of 1.9 mm can be assumed. A single cable itself consists of 28 winded strands, with a strand diameter of 1.065 mm. To place the two temperature sensors (Cernox® CX1050 type, bare chip HT) a strand is respectively manufactured out of the sample along the symmetry plane in the middle (see figure 19). The electric connection to the bare chip of the temperature sensor is prepared with a twisted four-wire Manganin cable (Copper-, Manganese- and Nickel alloy) to reduce a self-heating in the cable due to the induction of the coil and reduce the thermal contact to the outer helium bath. The void, created by the milled-out strand, is filled up with a tube surrounding the temperature sensor instrumentation cable.

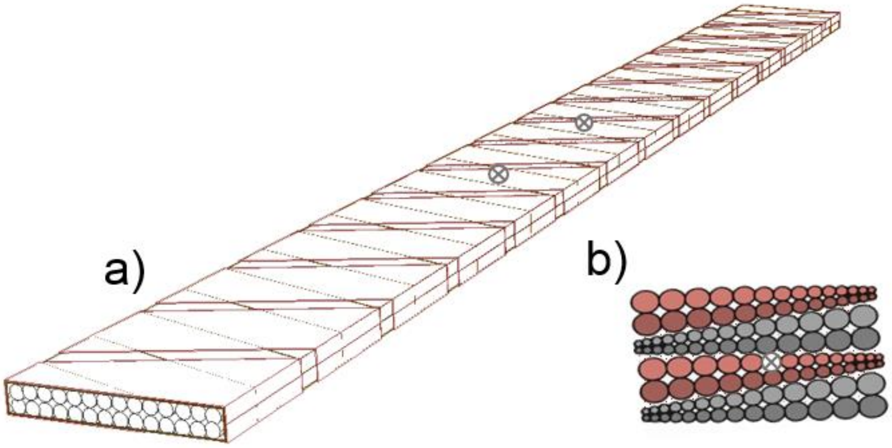

Figure 19: a) Single insulated Rutherford cable used for creating the cable stack of the sample, the two temperature sensors are marked with a cross-dot. b) Schematic illustration of the cable stack. The height ratio is not proportional to highlight the trapezoid shape of the single cables. The cross-dot marks the position of the temperature sensor.

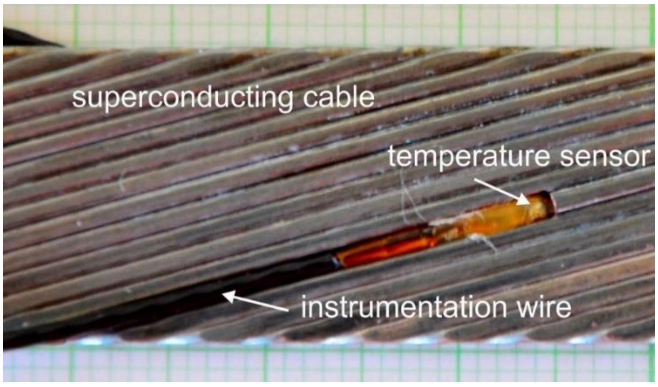

Figure 20: Single cable photographed during the sample preparation without the insulation. The temperature sensor is glued with epoxy to assure a proper thermal contact to the cable-strands and disable a direct liquid helium cooling in the void.

3.3 Calibration of the set-up

3.3.1 Induced heating by the coil on the sample

The heat in the sample is generated by powering the superconducting solenoid magnet with alternating current and the generated changing magnetic field couples to the interstrand resistance. Two methods to calibrate the provoked heat in the sample have been performed.

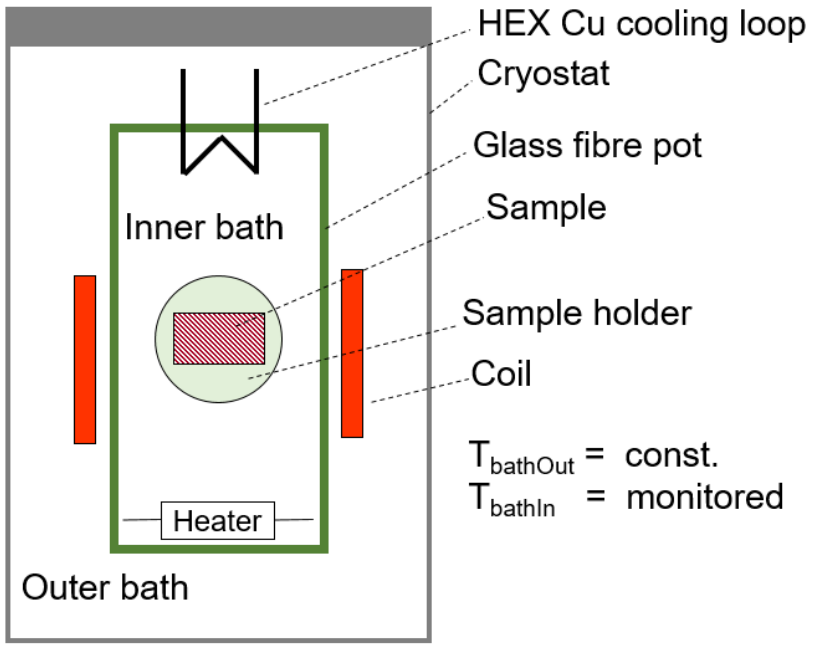

Figure 21: Schematic illustration of the mechanical set-up for the calorimetry of the heat deposit in the sample.

The first calorimetry used an adiabatic method, where the sample is decoupled from the environment. A detailed knowledge of the heat capacity is necessary to calculate the deposited heat per volume with this method, but the results of this investigation showed an insufficient uncertainty [22]. Hence, a further calorimetry with the principle of a heat meter was performed.

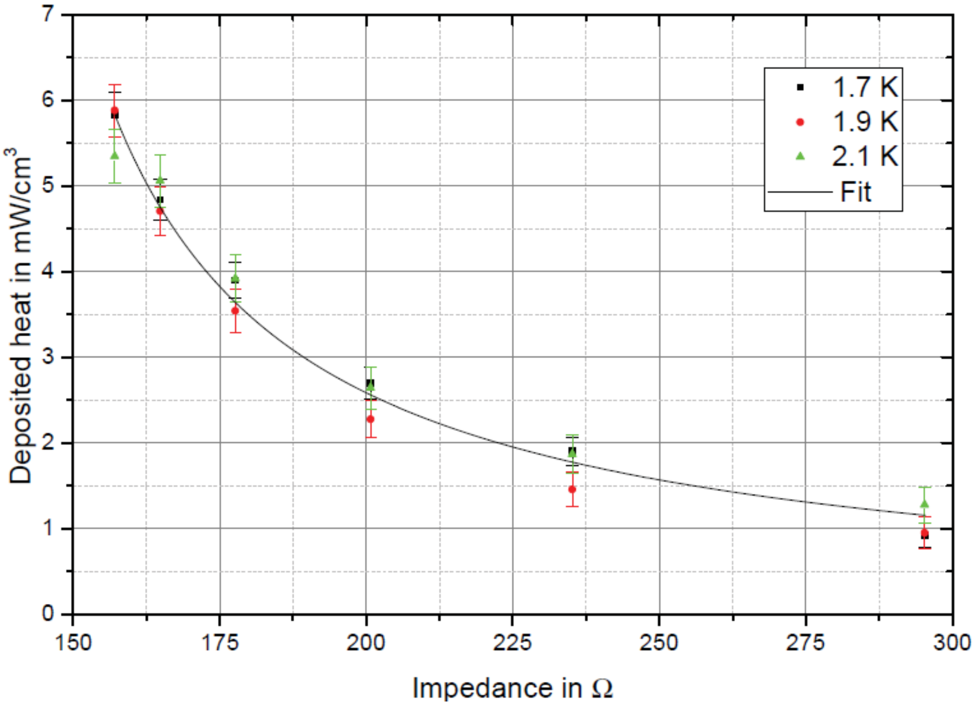

Figure 22: Deposited heat in the sample in relation to the impedance of the coil, reprinted from **[23]**.

The pot and the cryostat are filled with liquid helium for the calorimetry. The pressure in the cryostat is regulated and kept on steady conditions with the corresponding saturation temperature. The principle of a heat meter requires a thermal barrier within the heat flow. In this set-up, the thermal barrier can be seen as the pot and the heat exchanger copper tube, which has a temperature gradient during the heating.

The temperature gradient behaves proportional to the heat flux. To determine the deposited heat in the sample a characterization of the heat meter has to be made. For this reason, a resistive heater is placed in the pot and powered with a controlled source. The temperature of the outer- and inner bath are observed and characterized in respective to the resistive heater. To set this in relation with the provoked losses in the sample the coil is triggered with a controlled impedance. To exclude in the calorimetry losses in the sample holder, two runs with a triggered coil were performed, one with the sample and the other one without. The measured temperature difference of these two runs was subtracted from each other to obtain simply the temperature difference generated by the sample. Figure 22 shows the relation between the impedance of the coil and the dissipated heat in the sample. The cable geometry in this graph was considered to determine further values per cable unit.

3.3.2 Temperature sensors

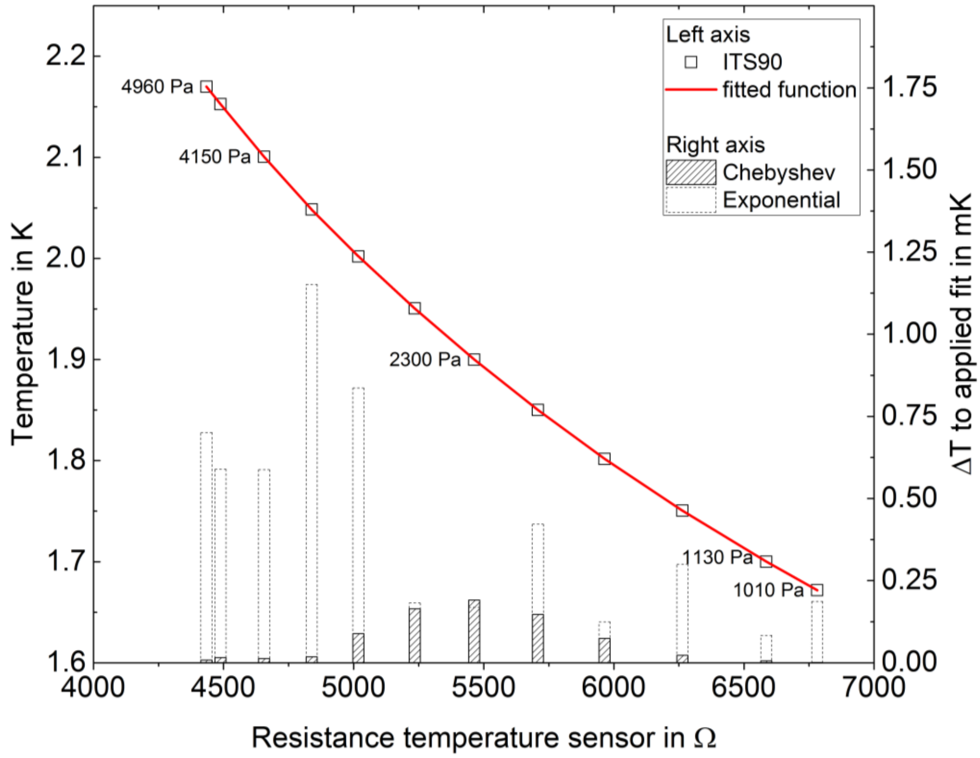

Figure 23: Calibration curve of the 75 MPa unified measurement set. The influence of the applied fit function is illustrated with the right y-axis. The pressure values are the respective liquid helium bath pressures.

The calibration for the temperature sensors is realized for every measurement set to exclude the influence of a varying resistance in the measurement chain of the temperature sensors. The uniform temperature in helium II allows a calibration of the sensors via a controlled pressure, thus the saturation curve of helium gives the temperature. The definition of the temperature is taken from the international temperature scale of 1990 [24]. The temperature sensors were exposed in a liquid helium bath and the voltage drop was recorded on steady state pressure conditions. The applied pressure transducer has an uncertainty of 0.25 % of reading and the current-source meter of the sensors 50 pA. Thus, an absolute error of the temperature reading results remains below 0.2 mK. The calibration curve was realized with a Chebyshev polynomial 8^{th} degree and fitted with a non-linear-least square method. The Chebyshev polynomial was chosen over an exponential function as the deviation of the calibration points to the fit curve showed up to an order of magnitude more precise results in the fitted data range as it is illustrated in figure 23.

3.4 Measurement conditions

The performed measurement campaigns had three kinds of mechanical configurations, further explained in the following sections.

3.4.1 Pot configuration

The standard configuration simply comprises the sample in a helium bath with saturated conditions. It has to be pointed out that the cryostat is initially filled with liquid helium and measures from the surface of the helium bath to the sample position a static height of 800 mm. This static height effects a static pressure on the helium at the sample position. Within the measurements, the helium evaporates and the height of the bath decreases. The static height of the bath is monitored and a static height > 400 mm is assured.

The second configuration within a measurement campaign includes the glass fiber pot surrounding the sample (see figure 17). The pot is equipped with a safety valve. This configuration, further called pot saturated, keeps the safety valve open and thus a liquid connection to the outer bath is warranted. Hence, the standard configuration and the pot saturate configuration appear only different in the presence of the pot.

The third configuration keeps the safety valve closed allows with a piping connection a pressurizing of the pot. This configuration will be called pressurized within this thesis.

3.4.2 Mechanical pressure

To imitate the mechanical pressure in the sample, a designed clamping structure applies a pressure. The effect of applying mechanical pressure on the sample was investigated in this study. To apply a mechanical pressure to the sample a tightening procedure for a designed clamping structure is developed.

The clamping structure is designed out of glass fiber material and non-magnetic steel to reduce self-heating. Six screws transfer via saucers the force to a glass fiber spacer which is placed on the sample. In initial measurement sets the saucers were not mounted and a localized pressure was provoked to investigate the influence. The calibration for the applicable mechanical pressure was performed with a copper block and attached strain gauges. Copper is a well-studied material and the properties and the geometry of the copper block are known.

With the help of this information the relation between the torque of the screws in the sample holder and the applied pressure was developed. The calibration to this procedure was performed at room temperature, 80 K and 4.2 K to standardize the tightening procedure of the screws for the mechanical sample pressures 30 MPa, 50 MPa and 75 MPa.

Experimental results

This chapter covers the interpretation of the measurement and discusses the outcomes of related research groups.

4.1 The experimental campaigns

The evolution of the experiment is illustrated in figure 24 with respect to the configuration. The initial measurement started with a testing of the influence of open cable ends. A vast opening permits the helium to enter the ends bypassing the polyamide insulation, which results in an over cooling of the cables. The further measurements were performed with a glass fiber piece sealed with epoxy to accomplish closed ends of the cables and follow the actual purpose of the measurements. The subsequent measurement sets investigated the influence of the mechanical sample pressure, as well as the pressure in the liquid helium. The first recorded sets had no saucers between the glass fiber spacer and the screws. Driven by an investigation to the heat treatment of the sample, the sample was separated from the glass fiber spacer after the 75 MPa localized set. At the interface cracks in the spacer have been revealed. The appearance of the cracks in the spacer, and the associated localized pressure on the sample are expected from the measurement set 75 MPa localized pot onwards. After the localized mechanical pressure on the sample was identified, saucers have been designed and implemented in the clamping structure to unify the pressure.

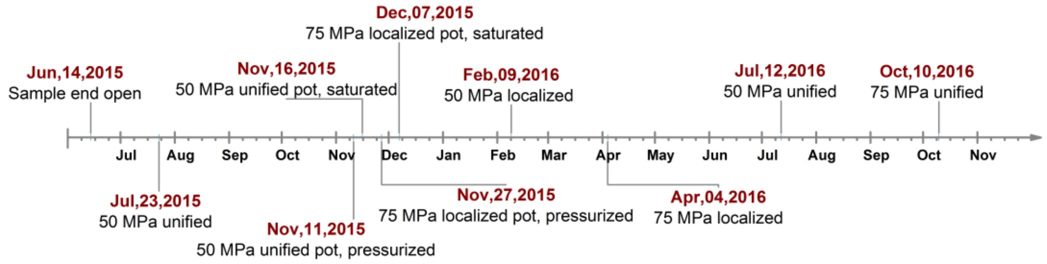

Figure 24: Timeline of the measurement sets with the different mechanical pressures and pressure distribution on the sample (unified localized). The liquid helium pressure is indicated by pot, which enables pressurized or saturation vapor conditions.

4.2 State of the art

Numerous experiments have been performed about heat deposition in fine helium channels and the cooling performance of He II with superconducting cables.

The Gorter-Mellink coefficient has been investigated for fine channel diameters from 0.102 m to $4.81 \cdot 10^{-3}$ m ($4 \cdot 10^{-3}$ m length) and annular channels by Kimura [25] for a bath temperature of 1.9 K with pressurized helium. The results of this experiment revealed the independency of the Gorter-Mellink coefficient from the geometry. Thus, a dependency of the Gorter-Mellink-coefficient exclusively from the temperature is valid for further discussions also for complex cable geometries.

An extensive review about the thermal resistances of the insulation schemes of the inner MB-cable of the LHC is given by La China et al. [26]. An analytic model, which implements the permeability of the superfluid helium through the insulation has been presented in this publication. However, the model is based on measurement data of C. Meuris [9], but the performed measurements to the porosity of the insulation can be valuable to future modelling.

A detailed numerical model of the inner MB cable with the enhanced insulation scheme has been developed with a 3-D geometry by Bielert [27]. The simulation agrees with the measurement results of Granieri [8], who performed measurements with thermocouples on a hand wrapped polyamide insulated cable.

As briefly mentioned, measurements are presented by C. Meuris, who investigated different insulation schemes with a heater [9], as well as with a cable mock-up using Joule heating [28]. The used Allen Bradley type sensors were embedded in epoxy resin and the cables were hand wrapped.

Similar to the experiments of C. Meuris [28], Kimura investigated the quadrupole cable [29]. He specifically states in detail the decoupling of the instrumentation and presents in the results a laminar regime for a low heat input > 1 mW/cm^3.

4.3 Data evaluation

A single measurement reads time dependent the sample temperature. The pressure in the helium bath is controlled and monitored to guarantee steady conditions surround the sample. When the magnetic field is triggered and provokes losses in the sample, a constant heat is applied to it. Thus, the time derivative of the energy equation (19) can be considered as constant (20).

$$\frac{\partial q}{\partial t} = c_p \cdot \frac{\partial T}{\partial t} + h \cdot A \cdot \partial T \qquad (19)$$

$$\frac{\partial Q}{\partial t} = const. = \dot{Q} \qquad (20)$$

The general solution of the ODE leads directly to the parameter τ (equation (21)), which allows to characterize the transient behavior of the sample.

$$\tau = \frac{c_p}{h \cdot A} \qquad (21)$$

Combined with the particular solution, the ODE gives the fit-function to the measurement curve and provides with its fit parameter an evaluation of the recorded measurement data. The used fit function is presented in equation (22).

$$T(t) = T_0 \cdot e^{\left(-\frac{t}{\tau}\right)} + \left(1 - e^{\left(-\frac{t}{\tau}\right)}\right) \cdot T_{eq} \qquad (22)$$

The sum square error of the applied fit is <5·10^{-3} s for the measured heating powers > 1.18 mW/cm³ at the measurement set 75 MPa with unified pressure. The evaluation for the fit of the lower heating powers showed no satisfactorily results due to the time resolution of the measurements with 20 ms.

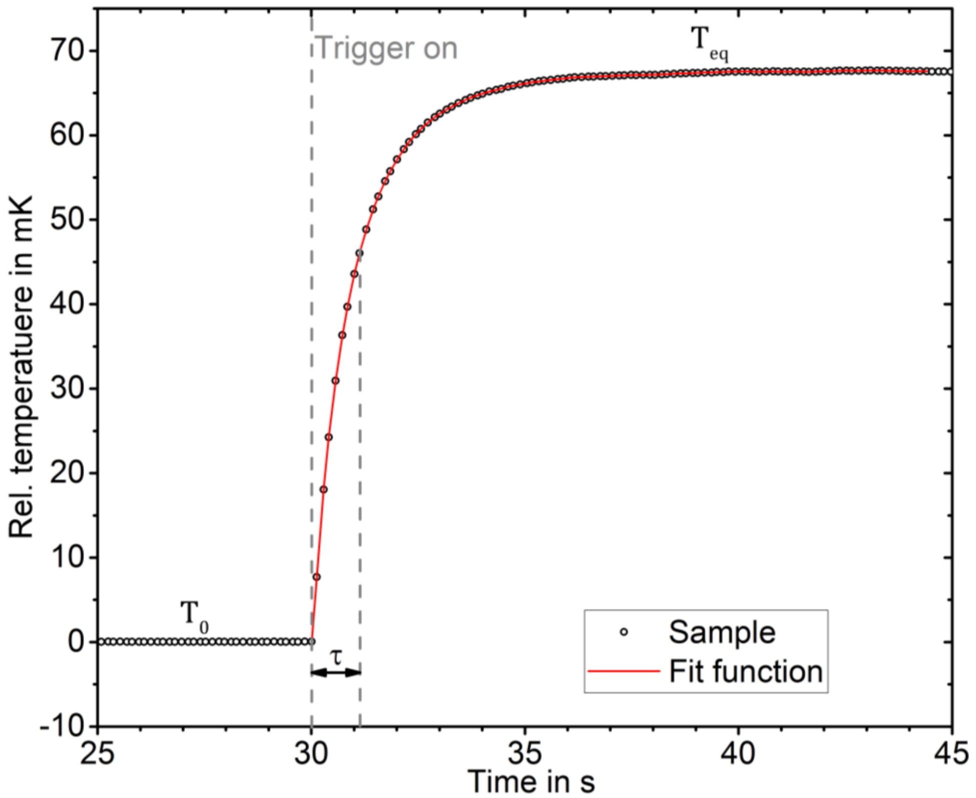

Figure 25: Characteristic measurement curve of the experiment at 1.9 K and 5.8 mW/cm³ heating power

The data evaluation takes place with an automatized code that compiles the initial steady state temperature T_0, the τ parameter and the steady state temperature during the heating T_{eq}. When the magnetic field is deactivated, the fit function of (22) follows the temperature decrease. The fit-parameter of the cooling down of the sample are recorded, too, as well as the steady state temperature after one trigger cycle.

4.4 Measurement results and interpretation

Within the evolution of the set-up several measurements have been performed. The latest measurement guarantees a more unified mechanical pressure than the previous ones. However, the influence of the local pressure will be discussed.

A general trend in the measurement sets showed a decreasing ΔT from a bath temperature of 1.7 K to 2.0 K. At a bath temperature of 2.0 K a minimum of the temperature increase is clearly visible and from this point on ΔT rises the higher the bath temperature gets. The described behavior is more pronounced to a higher heating power in the cable. In figure 26 the dependency of the heating power and the bath temperature to the temperature in increase is illustrated. It reflects the expected cooling behavior of He II in Gorter-Mellink-Regime with the highest thermal conductivity function between 1.9 K and 2.0 K. That results in the smallest steady state temperature increase.

Furthermore, the influence of the static height of the bath is marked in figure 26 to assure not to cross the lambda line at the saturation curve itself. The measurements sets started with the highest bath temperature and a helium level of around 800 mm relative to the sample. The dotted lines mark the ΔT necessary to reach saturation for three bath heights. The height of the helium bath is recorded to respect this limit. The dot dashed line marks the ΔT to the lambda transition.

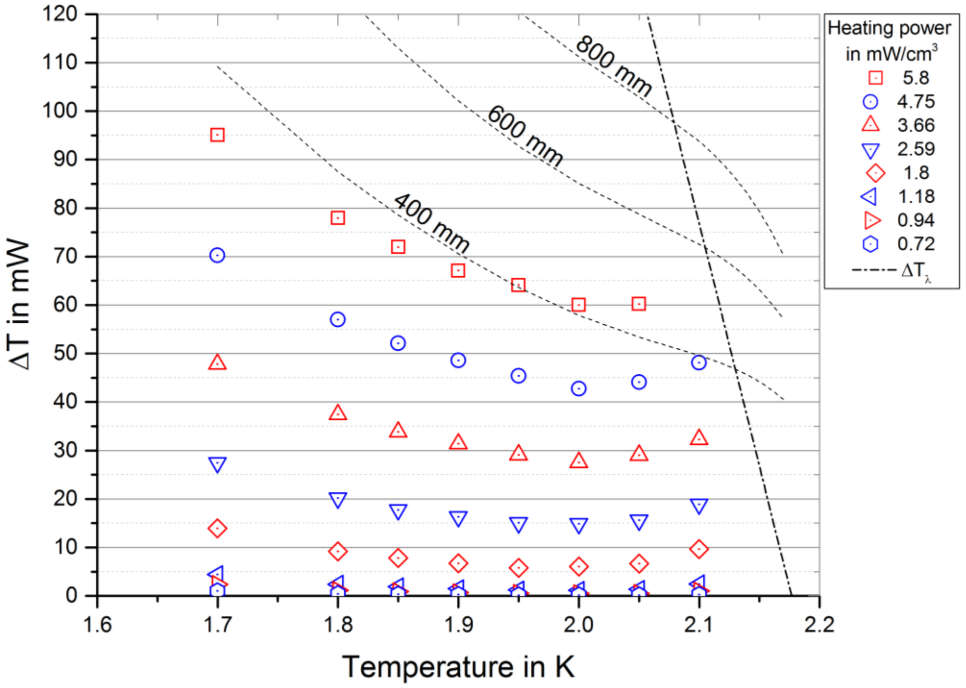

Figure 26: Temperature increase in a sample of the inner MB cable with an applied mechanical sample pressure of 75 MPa in a helium bath under saturation conditions. A slight subcooling of the liquid is caused at the sample due to the static height of the liquid column. This subcooling is a substantial contribution, since the absolute pressure of the helium bath is between 1050 Pa and 4950 Pa.

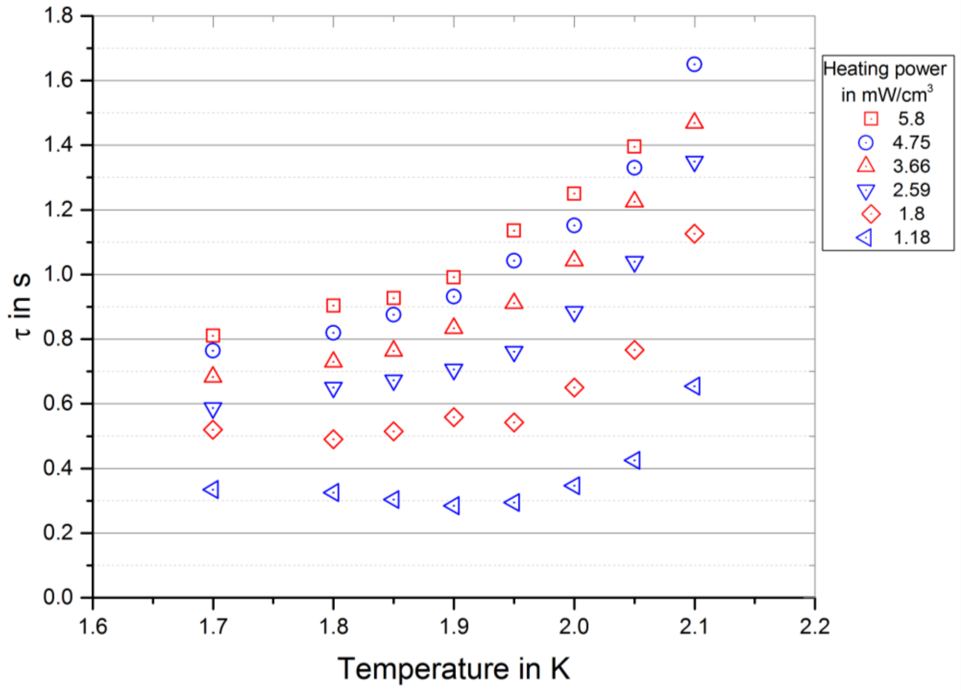

Figure 27: Fitted time parameter tau for the heating curves with 75 MPa sample pressure over the temperature in respect to the heating power in an instrumented sample of the inner dipole cables.

Figure 27 presents the fitted time constant to the rising temperature at the beginning of the heating pulse. Noteworthy is the different behavior of the tau-parameter for heating powers greater than 1.8 mW/cm³ with a constant rise in the time constant with the bath temperature. The smallest presented dependency of 1.18 mW/cm³ shows a qualitative interesting minimum around 1.95 K, comparable with the highest thermal cooling performance shown already in figure 26. The higher time constants for higher bath temperatures are caused by the drastic increase in heat capacity of the liquid helium towards the T_λ comprised in figure 10.

The ratio of $c_p/h \cdot A$ gives an indication to evaluate the slope of the heating curves. The measurement points for the low heating powers are not presented in the graph as the time resolution didn't allow a reliable fit due to the dynamic of the temperature increase.

To give a better guidance to the eye figure 26 and figure 27 are illustrated in a 3-D plot in figure 28 and figure 29.

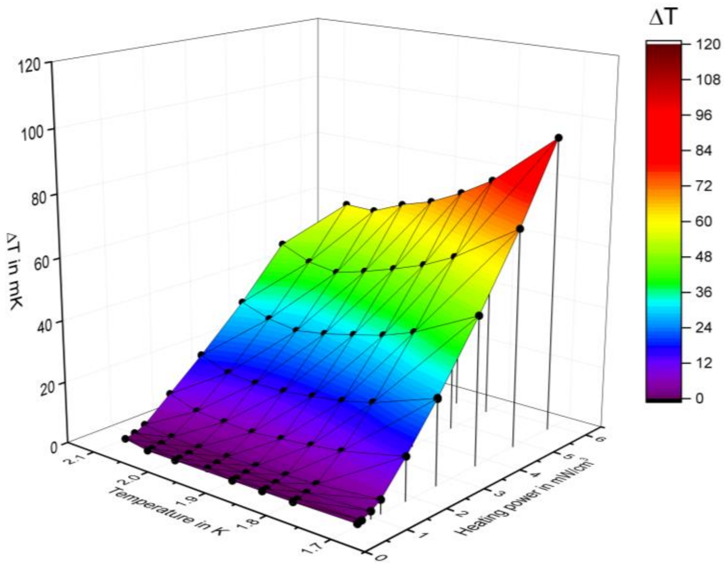

Figure 28: Measured temperature increase in the sample of the inner MB cable as a function of the bath temperature and heating power in a 3-D illustration with 75 MPa sample pressure.

The highest ΔT are reached for the lowest bath temperature and the highest applied heating powers. The highest measured ΔT for 5.8 mW/cm³ at 2.1 K did not reach stable conditions anymore. Furthermore, the transition to He I results in a steep temperature rise (not shown in the graph).

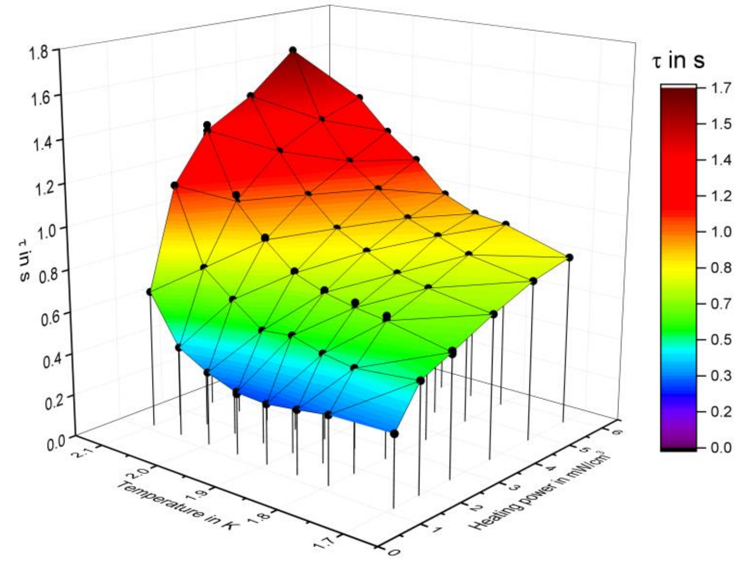

Figure 29: 3-D illustration of the fitted tau parameters to the instrumented sample of the inner MB cable in relation to the bath temperature and the heating power with an applied mechanical sample pressure of 75 MPa.

Figure 29 represents the shape of $c_p(T)$ for the liquid helium towards the transition of He I to He II. The sharp rise of c_p towards the λ-transition determines the time constant tau.

4.4.1 Interpretation of the low heating powers

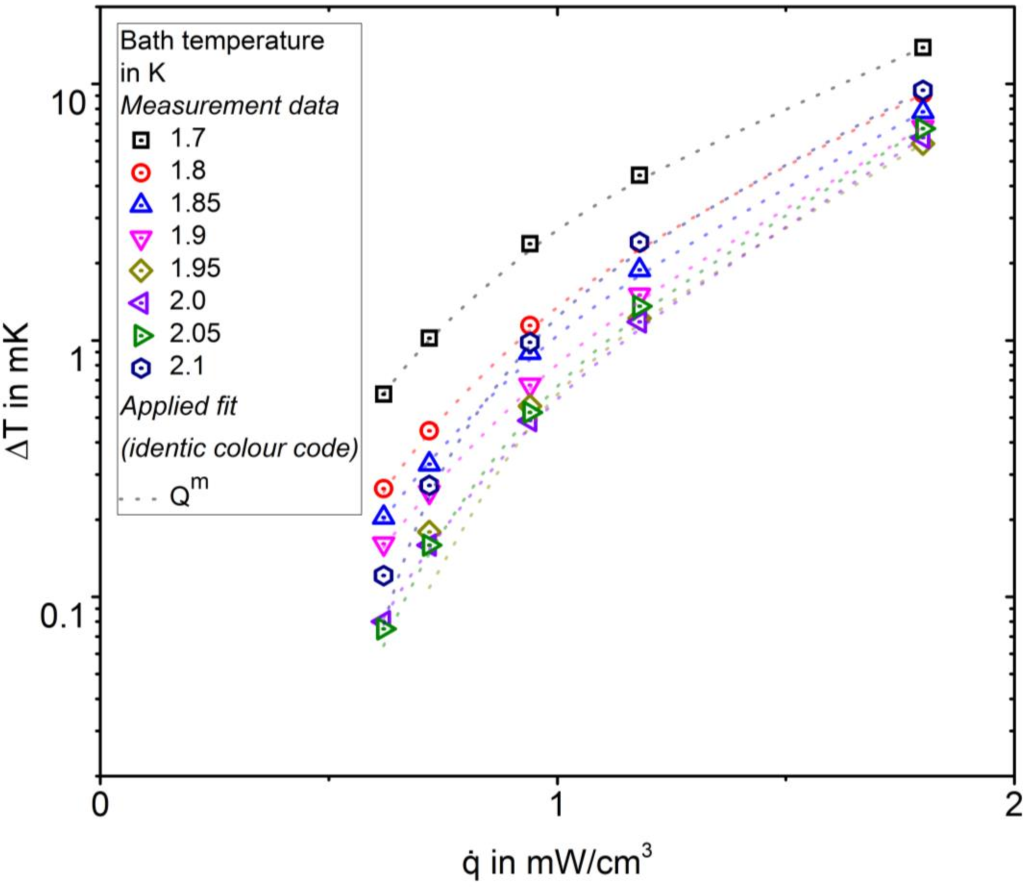

Figure 30: Measured temperature increase on a low heat input (q̇<1.8 mW/cm3) and the fitted function in dotted lines.

Figure 30 illustrates the temperature increase versus the heat input in the lower range. The temperature increase relates a close to cubic function of the heat input for a low q̇ <1.8 mW/cm^3. This behavior could be interpreted as a turbulent regime, as the exponent of the superfluid thermal conductivity function was found by several experiments around 3 [11]. A laminar regime with a linear heat-temperature increase relation was not observed in the measurement results. A laminar regime is expected at much the lower heating powers. The lowest heating power of 0.62 mW/cm^3 is measured with a temperature increase < 0.2 mK for the bath temperatures above 1.7 K. Thus, as conclusion could be revealed that for the lower heating powers a turbulent behavior of the helium is the dominant mechanism

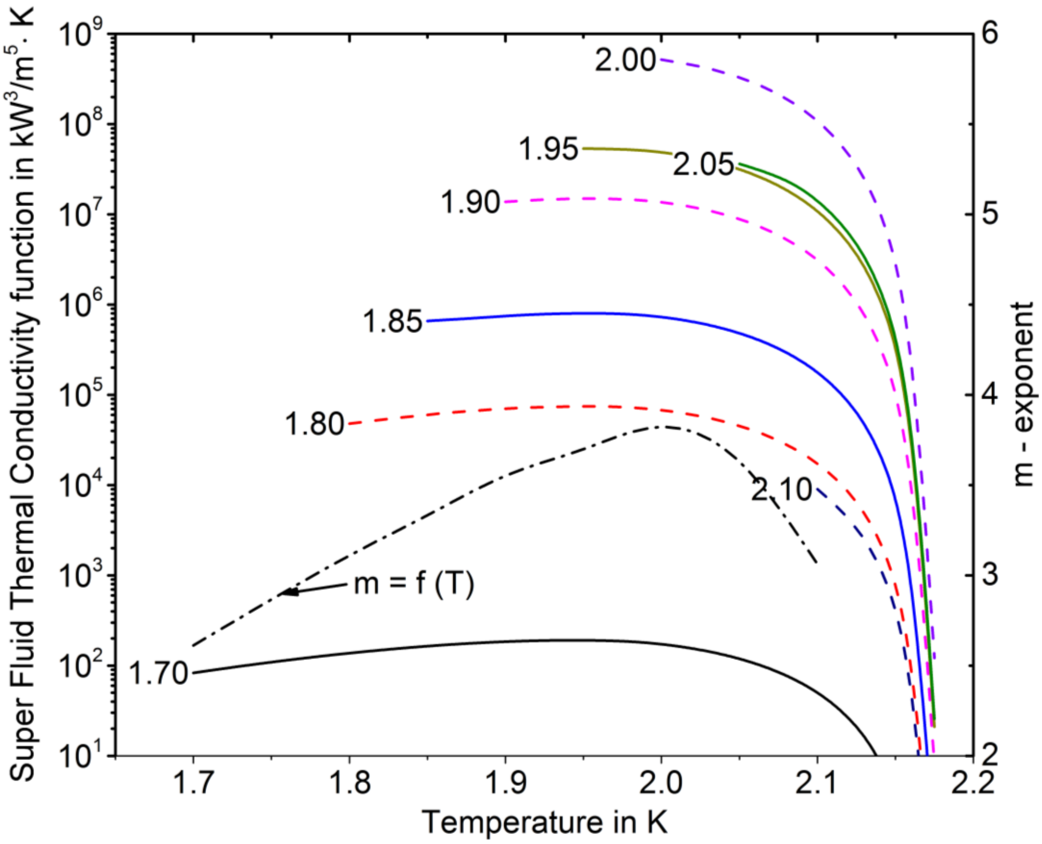

Figure 31: Calculated f^{-1}-function of the inner MB-cable for a low heating power ($\dot{q}$<1.8mW/cm3) versus the helium temperature in respect to the initial bath temperature labeled on the curves. The right y-axis shows the exponent of the superfluid thermal conductivity function, which was fitted to the experimental measurement values.

The superfluid thermal conductivity function is strongly dependent on the exponent. A fit of the measurement points was performed for each initial bath temperature with different heating powers. Figure 31 illustrates the superfluid thermal conductivity function versus the helium temperature with the fitted exponents in respect to the initial bath temperatures. It has to be pointed out that this behavior of the functions is exclusively considered for the low applied heat loads region. The initial bath temperatures are labeled on the curves, while the helium temperature is labeled on the x-axis. The right y-axis shows the fitted exponent of the superfluid thermal conductivity function as a function of the helium temperature.

4.4.2 Interpretation of the higher heating powers

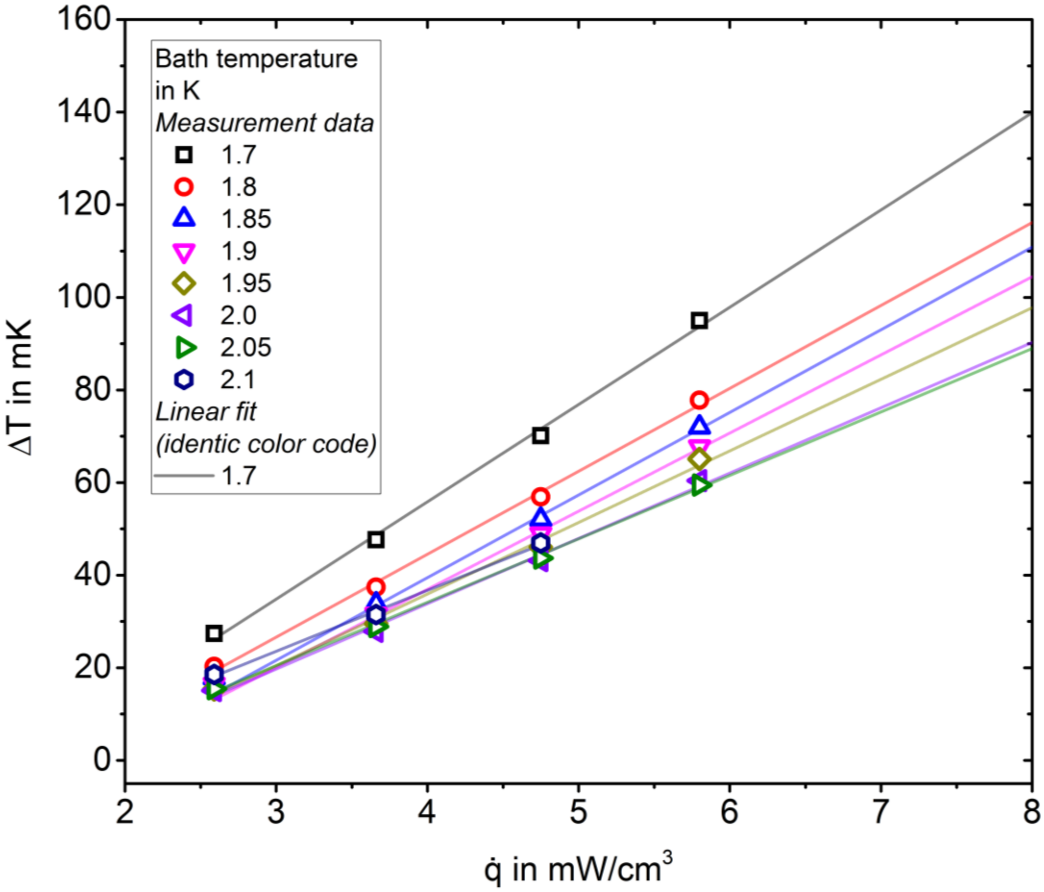

Figure 32: Measured temperature increase on a high heat input ($\dot{q}$>1.8 mW/cm³) and the fitted function in transparent lines. The color code of the bath temperatures used the same declaration for the data and the fitted functions.

The higher heat inputs are in the experiment observed to follow linear relation. Figure 32 illustrates the measurement points and the applied linear fit. The lower heat loads showed a cubic behavior, while the high heat loads region acted more in a linear relation. Thus, the cooling gets better towards higher heat loads. Initially an opposite behavior with a laminar region changing in a turbulent regime was expected. However, this could not be confirmed.

4.4.3 Observed behavior of the helium channels

The observed behavior indicates that different heat transfer paths are involved in the sample cooling. Geometry effects clear the Landau regime away so that the improved cooling for higher heat loads can be explained by a second helium channel.

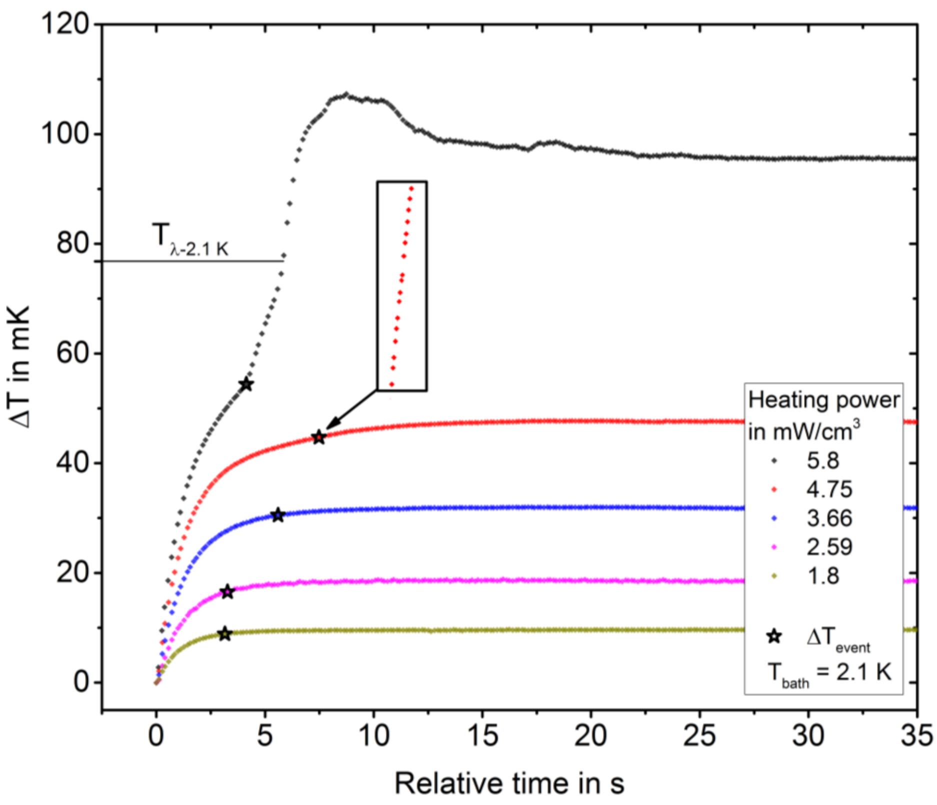

Figure 33: Temperature increase over the time for the single measurement runs in respect to the time at 2.1 K bath temperature and 75 MPa unified sample pressure. The stars mark an event in the temperature measurements.

A detailed view in the single measurements allows a further discussion. Figure 33 shows all measured heating curves for a bath temperature of 2.1 K. This bath temperature needs a lower heating power for a phase transition in the 75 MPa unified measurement set. The heating curve for 5.8 mW/cm^3 follows the previous described linear relation and changes abruptly to a steeper function till the lambda temperature. From the lambda temperature, onwards the cable temperature excesses and levels out to a static temperature corresponding to saturation conditions. The heating curves without a phase transition seem to follow the thermodynamic principles of paragraph 4.3 and rising up exponential. Nevertheless, a microscopic picture of the measurements reveal a discrete behavior. The measurement curve for 4.75 mW/cm^3 in figure 33 zoomed to a detail and shows the event of a discrete temperature increase. A linear relation between the ΔT at the discrete event and the heating power has been found, including the heating curves which show a phase transition. This behavior can be linked to a deactivation of channels at a certain applied heat. A dedicated experimental run with high heat loads is being prepared right now to study the highly interesting transition behavior to He I.

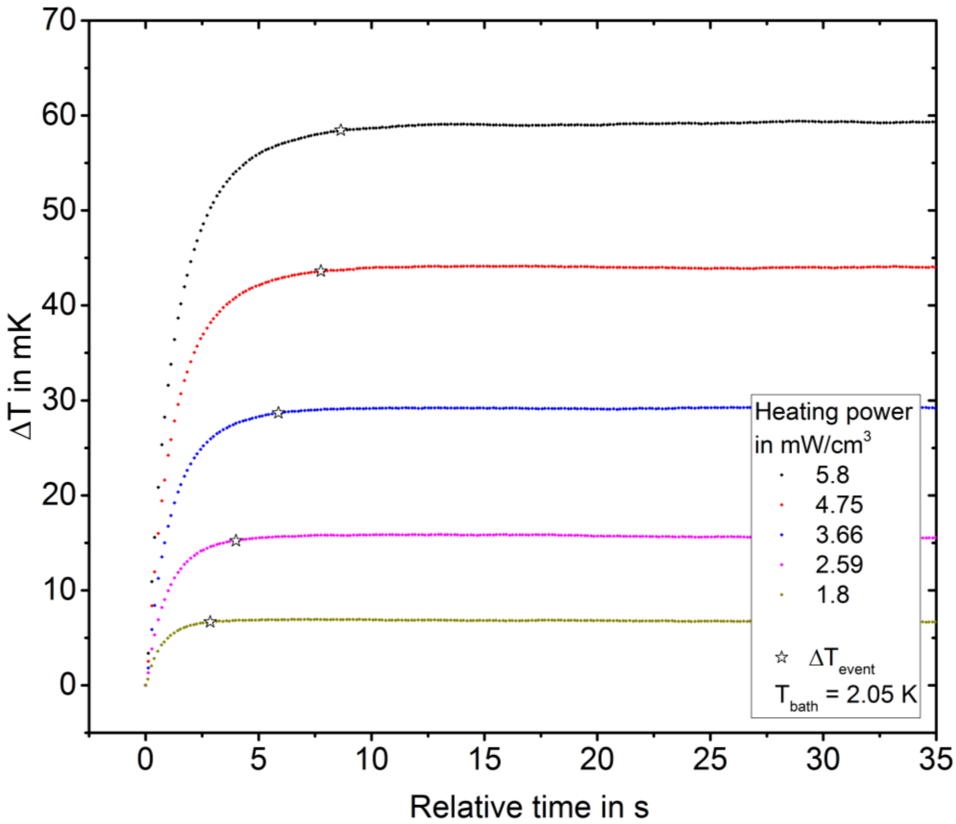

Figure 34: Temperature increase over the time for the single measurement runs in respect to the time at 2.05 K bath temperature and 75 MPa unified sample pressure. The stars mark an event in the temperature measurements.

In a heating curve without a crossing of the lambda temperature, this mechanism seems to be subdominant and plays a minor role for the higher heating powers. Thus, the heating curve is dominated below ΔT_{event} by an exponential behavior of the channels and changes above ΔT_{event} to at different function dependent on the dynamic of the exponential. The existence of the ΔT_{event} and a linear relation has been found at the date of the end of this thesis. Further experiments including higher heating powers with a foregoing simulation could verify this discovery.

The existence of the ΔT_{event} could be observed for all heating curves with a heat input >1.8 mW/cm^3. The existence of this event points on the lower heating powers was not clearly visible, which could be explained with channels that get more ineffective at a higher heating power. Another explanation for the non-seen event can be also the resolution of the measurement set-up. An observed existence of the events at a different temperature exclude an external measurement influence of the coil due to its cooling, that could possibly influence the magnetic field.

4.4.4 Comparison of the measurement data with the simulations

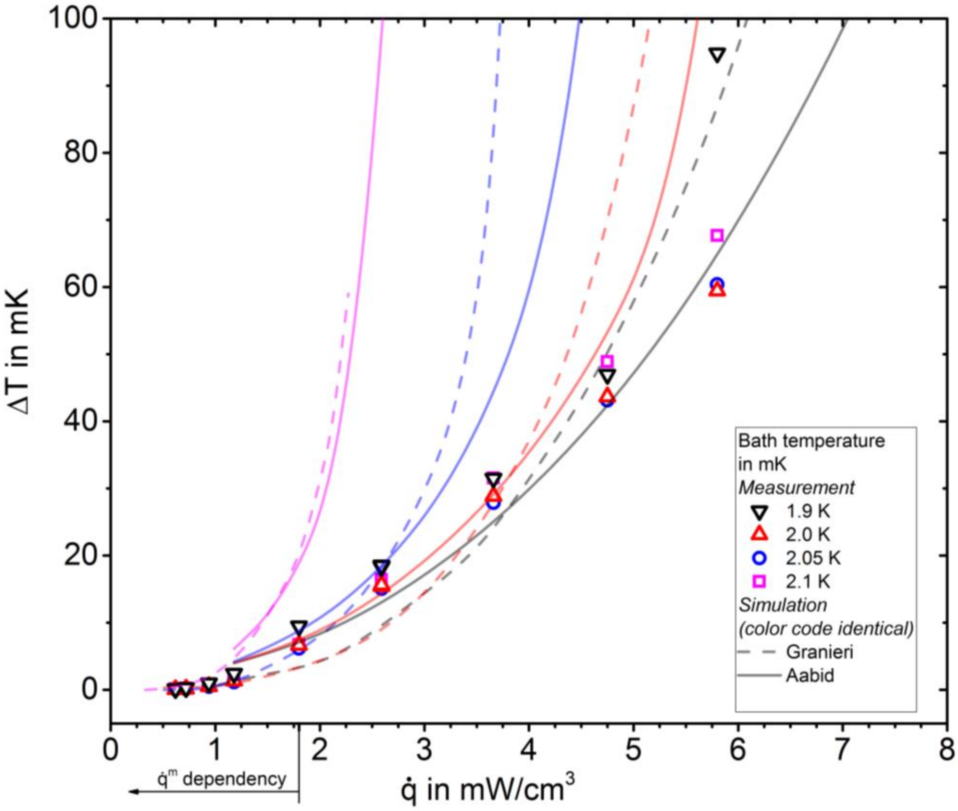

Figure 35: Measurement points at 50 MPa sample pressure compared to simulations of Granieri [8] and Aabid [30].

A numerical simulation has been performed in OpenFOAM by Aabid [30] in a collaboration. Figure 35 illustrates the results of this simulation in a full line with the experimental data in dots and the simulation performed by Granieri in a dashed line [8].

The OpenFOAM model abstracts the cable and considers no geometries, but simplifies the calculation to a coupled superfluid helium/solids multi-region system. The model follows the superfluid thermal conductivity function described in equation (15) with an exponent of 3. Thus, only the fluid parameters are considered and the simulation is dominated by a turbulent flow. An assumption of a helium/solid has been made of 0.03 % helium fraction and 0.03 % interfaces in the cable. Further boundary conditions were adiabatic side walls and the material properties of the Kapton® and the NbTi-cable.

The numerical simulation by Granieri [8] was performed with the complex geometry of the cable insulation. The simulation considered the different paths, where the helium could possibly exit the polyamide insulation. The model considered the fluid parameter for the Landau regime with a channel thickness of 6.64 µm, which were calculated with his measurements at 1.9 K. For the turbulent regime, the superfluid thermal conductivity with an exponent of 3 was used.

The measurements have shown, that the cable temperature follows a different behavior than the simulation. This could be explained with the dominance of the used factors of the turbulent fluid parameters.

The experiments showed the presence of helium channels, that get ineffective at some points. The models of Granieri [8] and Aabid [30] did not implemented this behavior. Hence, an improved modelling could be realized with a deactivation of channels that become dominant at an experimental detected function.

4.5 Interpretation of the possible measurement influences

This chapter discusses the influences of the mechanical pressure on the sample to the measurement campaigns and proposes a calibration method that was investigated to improve the accuracy of the applied mechanical pressure.

4.5.1 Reproducibility of the mechanical sample pressure

The performed measurements were reviewed to the hydrostatic pressure and the presented data are expected to be unaffected from any form of phase transition for the values below the lambda-point. A broader discussion allows the influence to the measurements with and without the pot configuration and the applied mechanical pressure, see figure 36.

The measurements are chronologically listed and the tightening process to apply the mechanical pressure followed an identic procedure. All the measurement sets are expected to have a unified pressure. The heating power was calibrated in the glass fiber pot; however, the two-other measurement sets in figure 36 are recorded without it. The pot is mainly designed out of glass fiber to reduce any decrease of the deposited heat in the sample. However, the cooling loop which is mounted on the top had to be realized out of copper to accomplish a temperature balance in the outer bath and in the pot.

The position of the cooling loop is 150 mm above the coil and 250 mm above the instrumented sample. Another criterion for the design of the pot, which had to be realized with a metal part was the leak-tight sealing. The sealing of the pot is implemented with indium.

The position of the sealing is 400 mm above the sample. Hence, this could not be a possible contribution to the measured lower ΔT with the pot configuration.

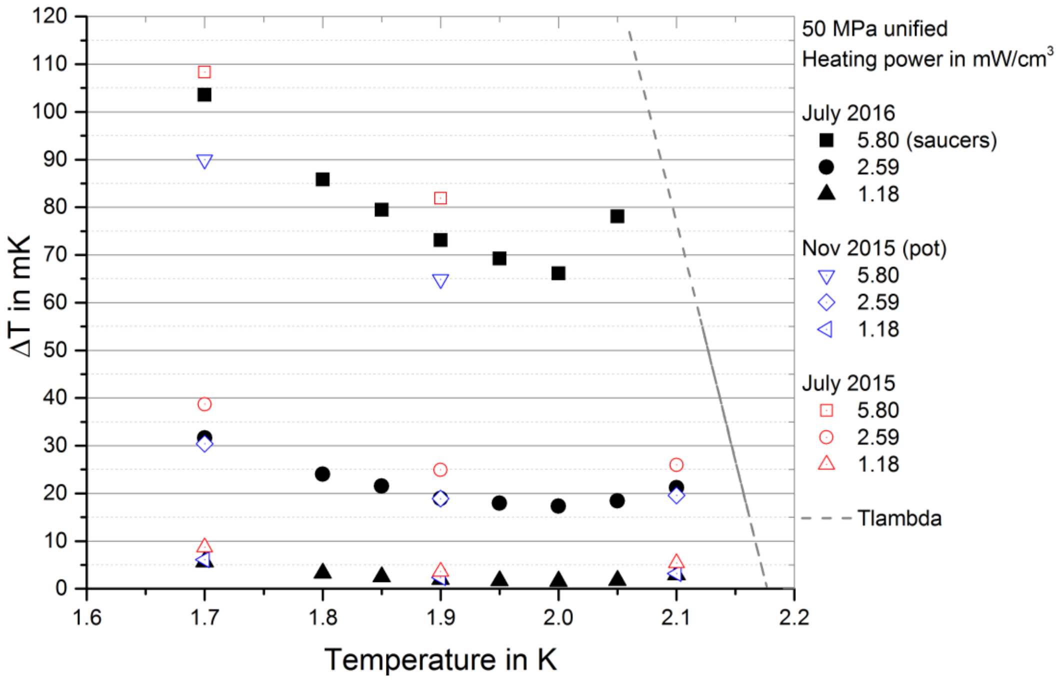

Figure 36: Comparison of the performed measurement sets with 50 MPa mechanical sample pressure. The measurements in July 2015 and 2016 had the same mechanical configuration, except the saucers. The measurement set of November 2015 was performed with the pot.

The reduced ΔT of the latest measurements could be influenced by the saucers, which were placed in the sample holder to unify the sample pressure. The saucers are optimized to transfer the mechanical pressure by the use of as less as possible material. The selection of the material had the criteria of a non-magnetic, resistive to low temperature and a low coefficient of thermal expansion. The stated criteria lead to the austenitic steel 1.4430. The saucers are placed in between the glass fiber spacer and the screws which maintain the mechanical pressure. The metallic part of the former measurement sets, close to the sample, is basically replaced by the saucers, as the screws moved up in position. This influence can be excluded with a further calorimetry of the heat deposition.

A variation of the applied mechanical pressure influences the temperature increase due to plastic deformation of the polyamide insulation. The tightening procedure to apply the mechanical pressure has been developed by T. Winkler, based on experiments, which were tested at a different temperature of 293 K, 80 K and 4.2 K with strain gauges on a copper block. However, a repetition of the experiment at room temperature showed for the given pressure a variation of the strain gauge resistance in the micro-Ohm range. Thus, an enhanced calibration for the applied mechanical pressure was investigated. To integrate the mechanical pressure over the sample-surface the capacity within the cable stack can be used to characterize the relation of the torque of the screws to the mechanical pressure at the sample.

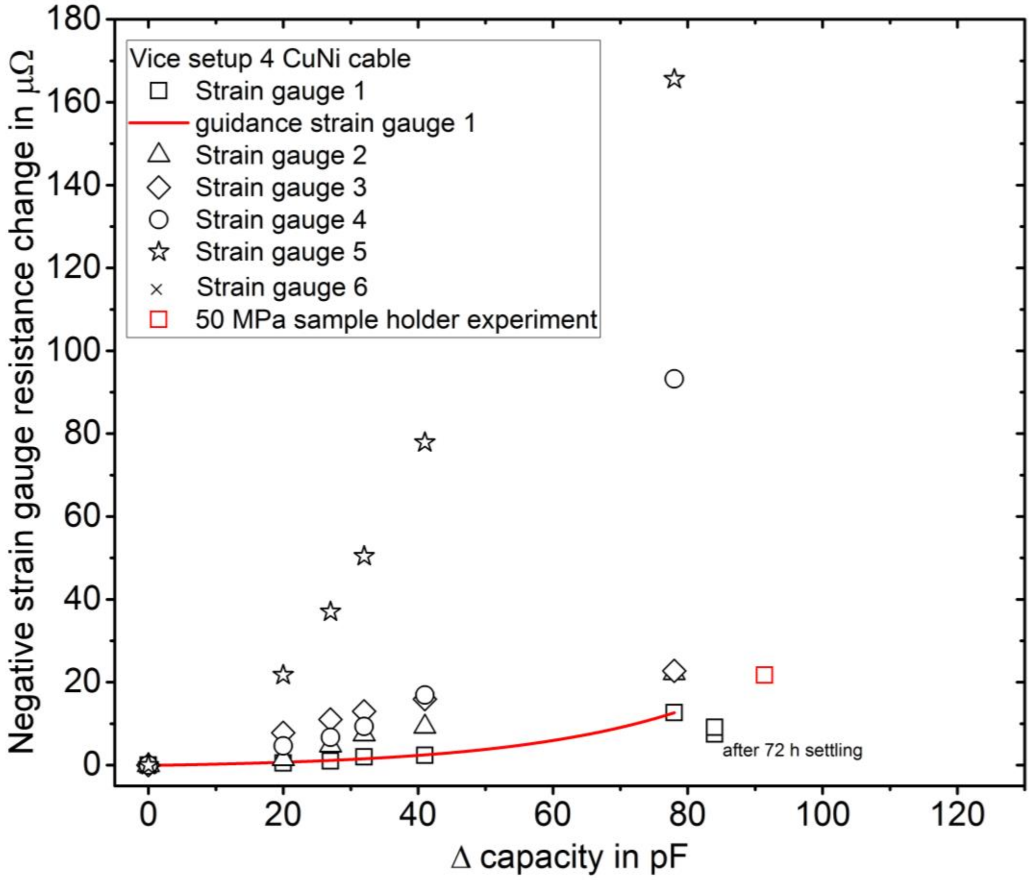

Figure 37: Composed structure out of four CuNi cables insulated with Kapton®, a copper block with six symmetric attached strain gauges and a glass fiber spacer. The capacity is measured in between the 4 cables. The graph characterizes the strain gauge resistance and the capacity with a rising applied pressure of the clamping structure. The two black squared measurement points at ~84 pF show the influence of the relaxation. The red squared point show the expected capacity for 50 MPa sample pressure assimilated to the red guidance line.

Figure 37 illustrates the characterization of the resistance of the strain gauges versus the measured capacity with an increasing pressure. Initially the position of the composed structure was varied to exclude a possible non-uniform pressure applied by the clamping structure. The variation of the position showed neither an influence to the strain gauge resistance nor the capacity. However, the resistance of the strain gauges within each other deviated in factor 10. The method of a capacity measurement for a pressure calibration seem under the light of figure 37 more appropriate. For a detailed characterization of the sample holder further tests can be performed at low temperature.

To attain a constant friction coefficient molybdenum disulphide is proposed to use during the characterization of the tightening procedure of the sample holder screws. A calibration for the sample in a cryogenic traction machine is under preparation.

4.5.2 Influence of the mechanical pressure deviation

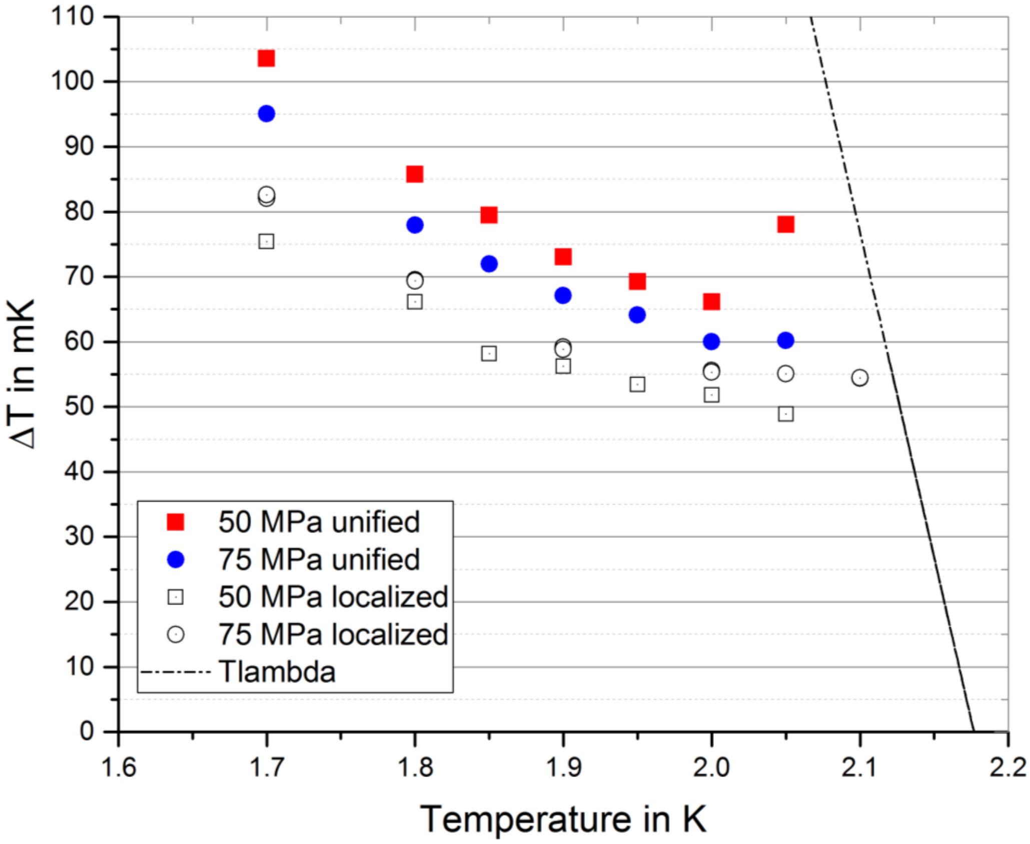

Figure 38: Temperature increase in a sample of the inner MB cable at a heating power of 5.8 mW/cm³ for different mechanical pressures.

A major factor of the temperature increase is the applied mechanical pressure. Less mechanical pressure leads to bigger helium channels and thus to a lower temperature increase, or to put it simply a lower sample pressure results in a better cooling.

Figure 38 illustrates the measurement sets in with a different mechanical pressure at 5.8 mW/cm^3 heating power. The data sets with the unified pressure do not match the previous described expectations. The behavior of a higher mechanical pressure followed with a higher temperature increase could be noticed for the measurement sets with a localized pressure. The uniform higher compression on the broad plane of the Rutherford cable can possibly enlarge helium channels in the side plane of the Rutherford cable. That can explain new cooling channels being available for a higher compression on the sample.

An interpretation of the localized pressure is linked to the pressure deviation. The helium channels next to the screws are expected to get smaller, but the surrounding channels should be larger and thus result in a better cooling than the unified pressure data sets. This behavior could be confirmed in the measurement data.

Increasing the sample pressure by 50 % leads on the lowest measured temperature to a difference of ~10 %. Within the measurement set the temperature increase seem to be consistent. A measurement with the same mechanical configuration could reveal the reproducibility.

A relevant factor for the measurements is besides the mechanical configuration the magnetic field of the coil. A monitoring of the magnetic field can be achieved by a Hall-Effect sensor, which transduces the magnetic field in a voltage signal. An evaluation of the produced magnetic field could exclude a discussion about a variation of the produced losses in the sample.

4.6 Comparison to other experiments

Superconductive cables were investigated by Kimura et al. [29] and Meuris et al. [28]. Both research groups used Joule heating to heat up the cable and measure the temperature increase.

The investigated cable by Kimura [29] measured the dimensions of the quadrupole cables in the LHC [5]. The temperature increase of the performed experiment and the work of Kimura measures similar values to heating powers >2.59 mW/cm^3, see figure 39. However, the lower heating powers were measured by the research group of Kimura with a different behavior, which was interpreted with a laminar regime and a linear relationship by this group.

The experiment, which was performed by Meuris [28] measured a similar trend to the measured data in this work. However, the heating power is shifted and it has to provoke more heating to achieve the same temperature increase. The paper of Meuris investigated different insulation schemes and illustrated for the heating power below 5 mW/cm³ only a measurement set with a different insulation scheme than the inner MB cable. Therefore, figure 39 illustrates with the crosses an insulation scheme close to the inner MB cable and with the diamonds a different one that was published with low heating powers. The black line was stated to have a cubic behavior, and thus interpreted as a turbulent regime. To the higher heating powers a better cooling can be observed, which can be also seen in our results. The two lowest measurement points of Meuris are interpreted as the laminar regime, which cannot be observed in our data.

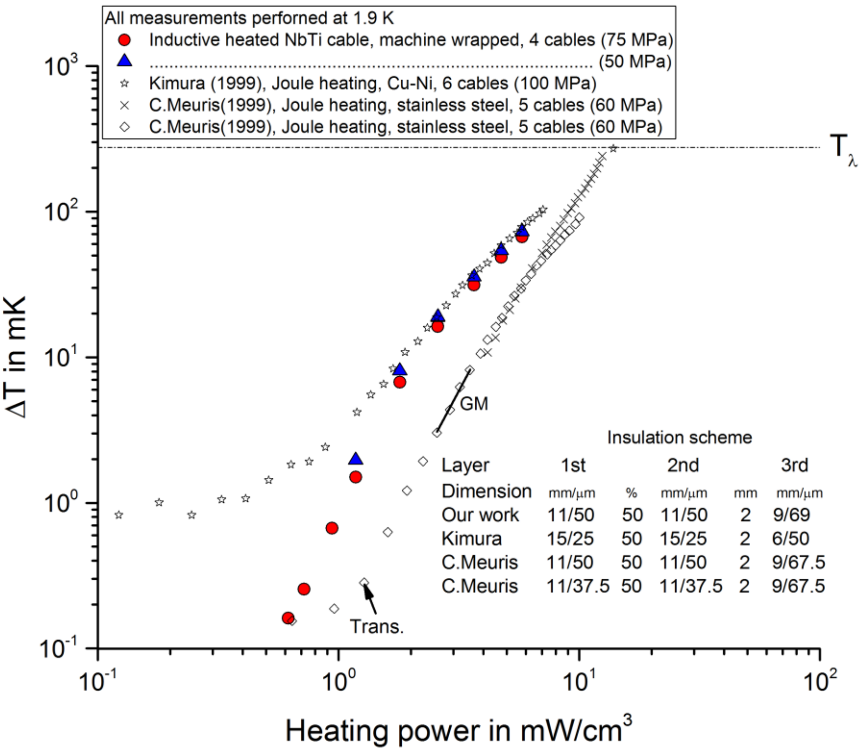

Figure 39: Comparison of the performed experiment with the work of Kimura **[29]** and Meuris **[28]**.

Figure 39 shows the trends of the measurements achieved by independent research groups. The data of Kimura show fluctuations to the lower heating power and can open a discussion to the limits of the temperature measurements or the provoked heat. The trend of the data from Meuris follows our observed behavior. A possible influence to the higher observed heating power of Meuris can be the conduction of the temperature sensors, which were attached on the sample. The high influence of the wrapping and the insulation scheme is evident.

Summary

Beam induced losses heating up among others the superconducting magnets in particle accelerators. The magnets of the main dipoles in the LHC are made out of NbTi cable embedded in a copper matrix and cooled with superfluid helium. The cables are insulated with a three-layer Kapton® insulation that allows the superfluid helium to enter in direct contact with the conductors. A detailed knowledge of the cooling mechanisms is needed.

A sophisticated measurement system has been developed at CERN by T. Winkler et al. [10] to investigate the cooling performance of superconducting cables. A sample of 4 machine insulated inner MB cables with two temperature sensors has been prepared and is placed in the measurement set-up. To provoke the losses in the sample a coil is placed around the sample in a cryostat. A glass fiber pot with a cooling loop can be placed in the set-up to allow a measurement in pressurized conditions. The calorimetry has been performed with an additional resistor placed in the glass fiber pot and the principle of a heat meter has been applied to determine the heating power in the sample. The calibration of the temperature sensors was achieved with saturation conditions of the helium bath and a pressure measurement. The measurements were performed from 0.62 mW/cm³ to 5.8 mW/cm³ at bath temperatures from 1.7 K to 2.1 K. The dynamics of the temperature increase was evaluated with a fit of the recorded temperature curve.

Possible influences to the measurements were investigated. For the actual heating power, saturated conditions in the set-up showed no influences compared to the pressurized measurements as the static height of the bath is creating sufficient subcooling to prevent for almost all cases a phase transition through the lambda line. An upgrade of the heating power in the set-up will achieve higher temperature increases, and thus the measurements should be performed in a pressurized helium bath. The influence of the mechanical sample pressure showed with an increase of 50 % an influence to the temperature increase of 10 %. However, measurements with the same mechanical sample pressure showed different temperature increases, which reveals the need for a better controlled sample pressure. Further measurements to calibrate the sample pressure with a capacity measurements were investigated and could improve the accuracy of the applied sample pressure.

The results showed for a heating power < 1.8 mW/cm³ a behavior of ~ $\dot{q}^3$ in relation to the temperature increase. This behavior could be interpreted as a Gorter-Mellink regime and therefore the proposal of a superfluid thermal conductivity dependent on the bath temperature has been made.

The heating powers >2.59 mW/cm³ showed a linear behavior of $\dot{q}^3$ to the temperature increase. Thus, a better cooling is visible for the rising heating powers in comparison to the cubic behavior below 1.8 mW/cm³. A dedicated measurement run is proposed to check the transition behavior towards He I for high heating powers.

A comparison with other experiments that investigated the heat deposition in superconductive cables verifies the measured results.

A novel mechanism of the cable has been observed in this experiment. A proposal for two channel openings has been made. In the measurements that have a temperature increase below the lambda point, only one mechanism is clearly dominant. If a heating of the cable provokes a temperature increase that comes close to the lambda point the other channel mechanism becomes dominant and the temperature increases vastly. A linear relation of the temperature rise and the heating power at the events where the first mechanism becomes sub-dominant was found and could help to simulate the events for intermediate heating powers. Further experiments with a higher heating powers, that could confirm this relation are planned as continuation of this thesis.

Outlook

The performed measurements during this thesis revealed the influence of the mechanical pressure on the sample. As discussed in section 4.5.1, a calibration for the applied mechanical pressure can be performed with a capacity measurement to improve the precision of the applied pressure at low temperature applied by the sample-holder over the sample. At the moment of writing this thesis, a traction machine with the possibility to operate at cryogenic temperature is in construction at the cryogenic laboratory at CERN. By the presence of this traction machine further investigations to the sample pressure can be performed.

The results of the measurements showed a discontinuity in the heating curve. Hence, a method to evaluate the dynamics of the heating curve could help to find relations that can forecast the moment where the behavior of the curve changes. To investigate this behavior further and to confirm the found relation of the temperature increase and the heating power, an increase of the changing rate of the magnetic field in the outer coil that provokes the sample heating is essential. At the moment of writing this thesis, first tests with the coil in alternating electrical current in two-phase operation have been made. The coil and the set-up are tested positive to withstand the higher voltage. The expected heating power was calculated and resulted in a factor three higher heating in the sample. To measure the higher heating power, a calorimetry has to be performed once more. A finer resolution of the high-power resistances to reduce the magnetic field could be valuable for the further measurements with higher heating powers. This adaption of the set-up would give an insight in the behavior below T-lambda, where the temperature increases drastically from the event discussed in section 4.4.3. The evaluation of this behavior could be also investigated beforehand with a further analysis of the dynamics of the heating curve. The transient behavior of the sample is just barely discussed in this thesis, as the current measurement set-up has a time resolution of 20 ms. To evaluate this matter more in detail, a faster measurement setup with a similar resolution has to be installed.

The actual sample was not cured with a heat treatment, as the heating during the measurements couples on the interstrand resistance. A heat treatment of the sample will reduce the interstrand resistance [31] and thus result in a lower available heating power of the system. After a detailed investigation in the previous discussed matters, a heat treatment of the sample could investigate the influence of the thermal curing of the sample to the cooling mechanisms of the cable, especially the Kapton® insulation.

Bibliography

[1] Communication Group, LHC the guide, Meyrin: CERN, 2009.

[2] X. Vidal and R. Manzano, "http://www.lhc-closer.es," [Online]. Available: http://www.lhc-closer.es/taking_a_closer_look_at_lhc/0.lhc_p_collisions. [Accessed 17 11 2016].

[3] G. Willering, "Stability of Superconducting Rutherford Cables for Accelerator Magnets," Twente, 2009.

[4] A. Verweij, "QUENCHES AFTER LS1," Chamonix, 2012.

[5] O. e. a. Bruennig, LHC Design Report Volume I, Geneva: CERN, 2004.

[6] CERN, "CERN CDS," CERN, [Online]. Available: https://cds.cern.ch/record/841539. [Accessed 17 06 2016].

[7] A. Ghosh and W. Sampson, "Minimum Quench Energy Measurements on Single Strands for LHC Main Magnets," vol. 9, no. June, 1999.

[8] P. Granieri, "Heat Transfer between the Superconducting Cables of the LHC Accelerator Magnets and the Superfluid Helium Bath," CERN, Meyrin, 2012.

[9] C. Meuris, "Heat transfer in electrical insulation of LHC cables cooled with superfluid helium," Elsevier Science Ltd., Gif-sur-Yvette, 1999.

[10] T. Winkler, "Development of a novel method for the exploration of the thermal response of superfluid helium cooled superconducting cables to pulse heat loads," Elsevier B.V., Geneva, 2015.

[11] S. W. Van Sciver, Helium Cryogenics, Florida: Springer Science+Business Media, 2012.

[12] CERN, "cern.ch," CERN, [Online]. Available: https://cds.cern.ch/. [Accessed 02 June 2016].

[13] www.cryodata.com, "HePack Version 3.4," Louisville.

[14] K. Atkins, Liquid Helium, Cambridge: Cambridge University Press, 1959.

[15] J. Wilks and D. Betts, An introduction to liquid helium, Oxford: Oxford scientific publications, 1987.

[16] V. Arp, "Heat transport trough helium II," *Cryogenics,* no. April, pp. 96-105, 1970.

[17] F. London, Superfluids Volume 11, New York: Dover Publications inc., 1954.

[18] C. Gorter and J. Mellink, "On the irreversible processes in liquid helium II," *Physica,* vol. 15, p. 285, 1941.

[19] W. van Alphen, G. van Haasteren and de Bruyn, "The dependence of the critical velocity of the superfluid on channel diameter and film thickness," *Physics letters,* vol. 20, no. March, p. 5, 1966.

[20] W. Vinen, "Mutual friction in a heat current in liquid helium II," The royal society mond laboratory, Cambridge, 1957.

[21] C. Chase, "Thermal Conduction in Liquid Helium II," Lincoln Laboratory, Massachusetts, 1963.

[22] T. Koettig, *Personal talk,* Meyrin, 2016.

[23] T. Winkler, "Calorimetry," Meyrin, 2016.

[24] H. Preston-Thomas, The International Temperature Scale of 1990, Ottawa: Metrologia, 1990.

[25] N. Kimura, "A Study on the Heat Transfer Properties of Pressurized Helium II through Fine Channels," in *Cryogenic Engineering Conference CEC Vol.51*, 2006.

[26] M. La China and D. Tommasisni, "COMPARATIVE STUDY OF HEAT TRANSFER FROM Nb-Ti AND Nb3Sn COILS TO HeII," Physical Review Special Topics - Accelerators and Beams 11, Geneva, 2008.

[27] E. Bielert, A. Verweij and H. ten Kate, "Finite Element Modeling in 3D of the Impact of Superfluid Helium Filled Micro-Channels on the Heat Transfer through LHC Type Cable Insulation," *IEEE TRANSACTIONS ON APPLIED SUPERCONDUCTIVITY,* vol. 22, no. 3, 2012.

[28] C. Meuris, B. Baudouy and D. Leroy, "Heat transfer in electrical insulation of LHC cables cooled withsuperfluid helium," *Cryogenics,* no. 39, 1999.

[29] N. Kimura and A. Yamamoto, "Heat transfer characteristics of Rutherford-Type superconducting cables in pressurized helium II," in *Applied Superconductivity Conference*, Palm Desert, 1999.

[30] F. Aabid, Interviewee, *Simulation of the inner MB cable in suprafluid helium 0.03% heliumfraction, 0.03% interfaces.* [Interview]. 06 11 2016.

[31] J. Nonte, Supercollider 4, New York: Plenum Press, 1992.

[32] VDI, VDI Wärmeatlas, 10. Auflage ed., Karlsruhe: Springer-Verlag, 2006.

[33] K. H. Grote, Dubbel Taschenbuch für den Maschinenbau 22. Auflage, Heidelberg: Springerverlag, 2007.

[34] IPU & Department of Mechanical Engineering DTU, "Coolpack," Lyngby , 2012.

[35] The National Institute of Standards and Technology, "REFPROP," Gaithersburg, 2007.

[36] G. Manfreda, "Review of ROXIE's Material Properties Database for Quench Simulation," CERN TE department, 2011.

Appendix

P&ID of the set-up

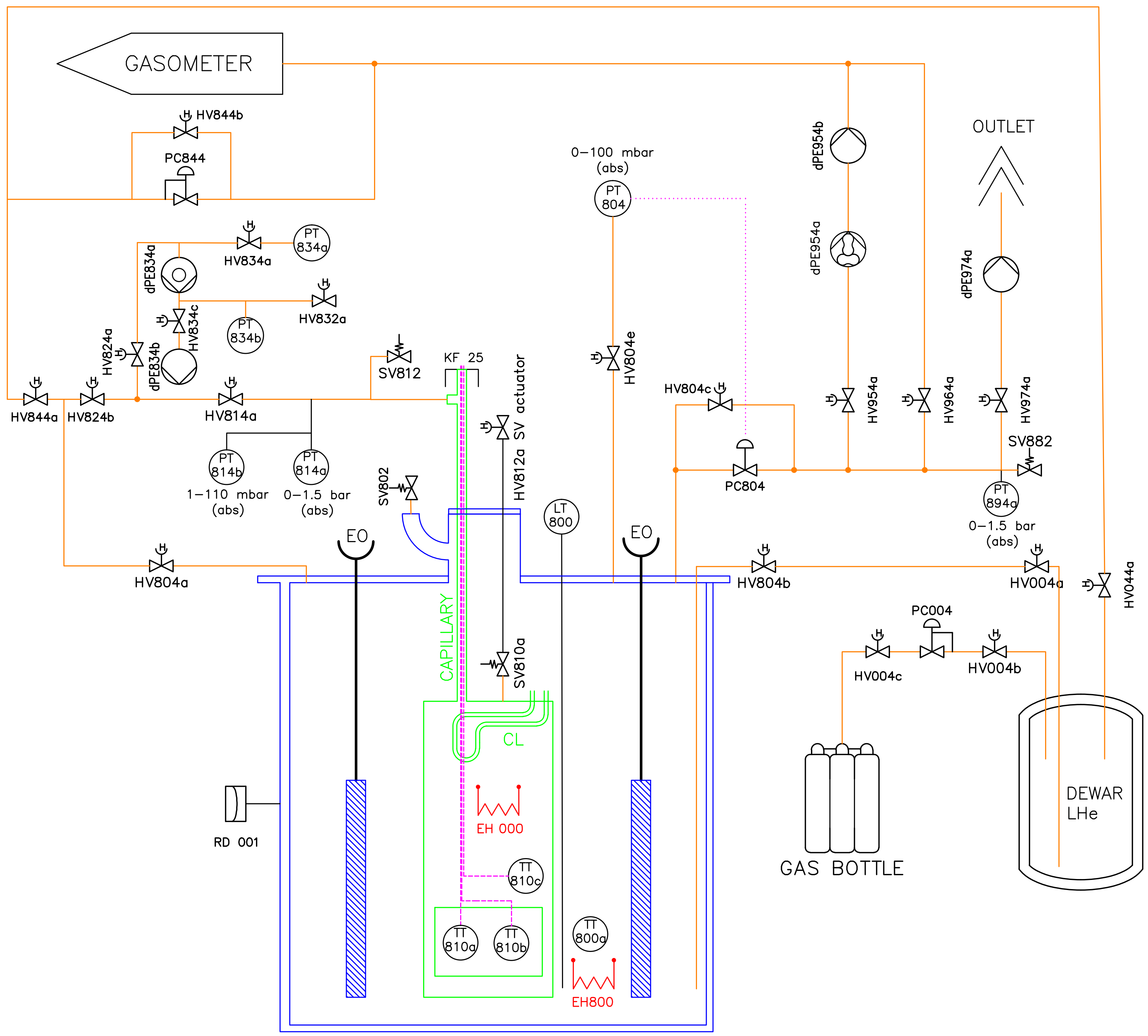

GASOMETER
HV844b
PC844
0–100 mbar
(abs)
PT
804
dPE954b
dPE954a
OUTLET
dPE974a
PT
834a
HV834a
dPE834a
HV832a
PT
834b
HV834c
HV824a
dPE834b
SV812
KF 25
SV actuator
HV804e
HV804c
HV954a
HV964a
HV974a
SV882
HV844a
HV824b
HV814a
PT
814b
PT
814a
1–110 mbar
(abs)
0–1.5 bar
(abs)
SV802
HV812a
PC804
LT
800
PT
894a
0–1.5 bar
(abs)
EO
EO
HV804a
HV804b
HV004a
HV044a
CAPILLARY
PC004
HV004c
HV004b
SV810a
CL
EH 000
RD 001
GAS BOTTLE
DEWAR
LHe
TT
810c
TT
810a
TT
810b
TT
800a
EH800

Matlab script for the data evaluation

```matlab
clear all;
clc;
close all;
format long;

%Folder where *.csv files are stored
folder='C:\Users\jschunde\01WorkJS\AnalysisThesis\2016-10-10-
75MPaUnified\C1Cbath\';
filename=dir(fullfile(folder, '*.csv'));
filename = {filename.name};
filename=filename';
Pressure=cellfun(@(str) str(19:22), filename, 'UniformOutput', false);
Pressure = Pressure';
Resistance=str2num(cell2mat(cellfun(@(str) str(29:31), filename,
'UniformOutput', false)));
Resistance = Resistance';
Heatinput=1./(-0.59571+0.00489*sqrt(157.09^2+power(Resistance,2)));
Resistance = cellfun(@(str) str(29:31), filename, 'UniformOutput', false);
Heatinput=num2cell(Heatinput)';
filename(:,2)=Pressure;
filename(:,3)=Heatinput;

%File name for the single measurement shown
cd(folder);
singleFilename={uigetfile('.csv')};
scriptName=mfilename('fullpath');
cd(fileparts(scriptName));

filename=sortrows(filename,[3,2]); %Sorting the files by heat input and
pressure, both ascending
Resistance=sortrows(Resistance,-1);
Resistance=str2num(cell2mat(Resistance));

%% Data import
numberOfFiles=size(filename,1);
numberOfFitPoints=100; %Number of points used for the fits

RowStart = 1; %First row of data
RowEnd = 3000; %End of data

ColumnTimeC1 = 6;
ColumnTempC1 = 9;

ColumnTimeCbath = 11;
ColumnTempCbath= 14;

Tlambda=2.1768;

FitCoeffC1=zeros(numberOfFiles,2); %Initialization of fit coefficient arrays
FitCoeffC1S4=zeros(numberOfFiles,2);
numberFilesDelete = 0;
opts = optimset('Display','off'); %No fit display on console

h = waitbar(0, 'Fitting results...');

for n=1:numberOfFiles;

files(n,1)=strcat(folder,filename(n,1));
Heat(n,1)=1/(-0.59571+0.00489*sqrt(157.09^2+Resistance(n)^2));

%File reading
timeC1(:,n) = dlmread(char(files(n,1)),'\t',[RowStart ColumnTimeC1 RowEnd
ColumnTimeC1]);
temperatureC1(:,n) = dlmread(char(files(n,1)),'\t',[RowStart ColumnTempC1
RowEnd ColumnTempC1]);

timeCbath(:,n)= dlmread(char(files(n,1)),'\t',[RowStart ColumnTimeCbath
RowEnd ColumnTimeCbath]);
temperatureCbath(:,n) = dlmread(char(files(n,1)),'\t',[RowStart
ColumnTempCbath RowEnd ColumnTempCbath]);

%Calculation of standard deviation of initial temperature's (200 points)
%noise, in Kelvin
standardDev(n)=std(temperatureC1(1:200,n));

%Zone detection, to detect the start of the temperature rise and the start
%of the temperature decay.
zoneCounter = 1;
diffTemp = abs(diff(temperatureC1));
tolDiff = 5*mean(diffTemp);
i = 1;
while i < length(temperatureC1);
    if diffTemp(i) > tolDiff;
        zonePoints(zoneCounter) = i;
        zoneCounter = zoneCounter + 1;
    end;
    i = i + 1;
end;

%startPositions(n) = zonePoints(1);

risingExp = zonePoints(zonePoints > 100 & zonePoints < 1000);
fallingExp = zonePoints(zonePoints > 1000);

%Average of the lowest and highest temperature plateaus
S1C1(n,1)=mean(temperatureC1(1:zonePoints(1),n));
S3C1(n,1)=mean(temperatureC1(risingExp(end):fallingExp(1),n));
```

```
%1st fit, rising exponential
timeC1rel(:,n)=timeC1(risingExp(1):risingExp(1)+numberOfFitPoints,n)-
timeC1(risingExp(1),n);
temperatureC1rel(:,n)=temperatureC1(risingExp(1):risingExp(1)+numberOfFitPoin
ts,n);

y = temperatureC1rel(:,n);
t = timeC1rel(:,n);
x0(1) = S3C1(n);
x0(2) = 0.5;
F = @(x,xdata)S1C1(n)*exp(-xdata/x(2))+(1-exp(-xdata/x(2)))*x(1);
[x,resnorm,~,~,output]=lsqcurvefit(F,x0,t,y,[],[],opts);

FitErrorC1(n)=resnorm/norm(y-mean(y))^2;
FitCoeffC1(n,:)=FitCoeffC1(n,:)+x;
x = [];
F = [];

%2nd fit, falling exponential
timeC1S4rel(:,n)=timeC1(fallingExp(1):fallingExp(1)+numberOfFitPoints,n)-
timeC1(fallingExp(1),n);
temperatureC1S4rel(:,n)=temperatureC1(fallingExp(1):fallingExp(1)+numberOfFit
Points,n);

y = temperatureC1S4rel(:,n);
t = timeC1S4rel(:,n);
x0S4(1) = S1C1(n);
x0S4(2) = 0.5;
FS4 = @(xS4,xdata)S3C1(n)*exp(-xdata/xS4(2))+(1-exp(-xdata/xS4(2)))*xS4(1);
[xS4,resnorm,~,~,output]=lsqcurvefit(FS4,x0S4,t,y,[],[],opts);

FitErrorC1S4(n) = resnorm/norm(y-mean(y))^2;
FitCoeffC1S4(n,:)=FitCoeffC1S4(n,:)+xS4;
xS4 = [];
FS4 = [];

% Mark the files with no HeII
k = 1;
testVariable = 0;
while k <= length(temperatureC1(:,n));
    if temperatureC1(k,n) > Tlambda;
        testVariable = 1;
        break;
    end;
%The calibration goes to 0 for T>Tlambda
    if temperatureC1(k,n) <= 0;
        testVariable = 1;
        break;
    end;
    testVariable = 0;
    k = k + 1;
end;

if testVariable == 1;
    numberFilesDelete = numberFilesDelete + 1;
    filesDelete(numberFilesDelete) = n;
end;

waitbar(n/numberOfFiles);

end

close(h);

% Deleting the points above Tlambda
files(filesDelete, :) = [];
filename(filesDelete, :) = [];
S1C1(filesDelete, :) = [];
Heat(filesDelete, :) = [];
S3C1(filesDelete, :) = [];
standardDev(filesDelete) = [];
FitCoeffC1(filesDelete, :) = [];
FitCoeffC1S4(filesDelete, :) = [];
FitErrorC1(filesDelete) = [];
FitErrorC1S4(filesDelete) = [];

%Saving the important results
Results(:,1)=S1C1;
Results(:,2)=Heat;
Results(:,3)=(S3C1-S1C1)*1000;
Results(:,4)=FitCoeffC1S4(:,2);
Results(:,5)=FitCoeffC1(:,2);
Results(:,6)=FitErrorC1'.*FitCoeffC1(:,2); %Fit error
Results(:,7)=100*abs(FitCoeffC1(:,2)-FitCoeffC1S4(:,2))./FitCoeffC1(:,2);
%Tau error
Results(:,8)=2*1000*standardDev; %error in temperature in mK
Results(:,9)=Results(:,2).*FitCoeffC1(:,2);
```

```
%Data sorting by heating power (062...072......580)
data=[round(Results(:,1)*100)/100,round(Results(:,2)*100)/100,round(Results(:
,3)*1000)/1000,...

round(Results(:,4)*10000)/10000,round(Results(:,5)*10000)/10000,round(Results
(:,6)*10000)/10000,...
    round(Results(:,7)*10000)/10000,round(Results(:,8)*10000)/10000];
data(:,9)=data(:,3)./data(:,5);
dataTemp=sortrows(data,[1,2]);

PT170=find(dataTemp(1:length(dataTemp),1)==1.70);
PT180=find(dataTemp(1:length(dataTemp),1)==1.80);
PT185=find(dataTemp(1:length(dataTemp),1)==1.85);
PT190=find(dataTemp(1:length(dataTemp),1)==1.90);
PT195=find(dataTemp(1:length(dataTemp),1)==1.95);
PT200=find(dataTemp(1:length(dataTemp),1)==2.00);
PT205=find(dataTemp(1:length(dataTemp),1)==2.05);
PT210=find(dataTemp(1:length(dataTemp),1)==2.10);

P062=find(data(1:length(data),2)==0.62);
P072=find(data(1:length(data),2)==0.72);
P094=find(data(1:length(data),2)==0.94);
P118=find(data(1:length(data),2)==1.18);
P180=find(data(1:length(data),2)==1.80);
P259=find(data(1:length(data),2)==2.59);
P366=find(data(1:length(data),2)==3.66);
P475=find(data(1:length(data),2)==4.75);
P580=find(data(1:length(data),2)==5.80);

dataTemp170=dataTemp(PT170(1):PT170(end),:);
dataTemp180=dataTemp(PT180(1):PT180(end),:);
dataTemp185=dataTemp(PT185(1):PT185(end),:);
dataTemp190=dataTemp(PT190(1):PT190(end),:);
dataTemp195=dataTemp(PT195(1):PT195(end),:);
dataTemp200=dataTemp(PT200(1):PT200(end),:);
dataTemp205=dataTemp(PT205(1):PT205(end),:);
dataTemp210=dataTemp(PT210(1):PT210(end),:);

data062=data(P062(1):P062(end),:);
data072=data(P072(1):P072(end),:);
data094=data(P094(1):P094(end),:);
data118=data(P118(1):P118(end),:);
data180=data(P180(1):P180(end),:);
data259=data(P259(1):P259(end),:);
data366=data(P366(1):P366(end),:);
data475=data(P475(1):P475(end),:);
data580=data(P580(1):P580(end),:);

Tsampling=1.9:0.02:2.2;
deltaTlambda=1000*(Tlambda-Tsampling);
```

```
%Plots
%deltaT vs. T for different Q
figure(100);
errorbar(data580(:,1),data580(:,3),data580(:,8),'pr','markers',12);
…
hold on;
plot(Tsampling,deltaTlambda,'-.k');
set(gca,'XTick', 1.6:0.1:2.2,'YTick',0:10:110);
axis([1.6 2.2 0 110]);
xlabel('\bf Temperature in K');
ylabel('\bf Temperature rise in mK');
title('\bf Evaluation Measurement - C1 Sensor');
legend('5.80','4.75','3.66','2.59','1.80','1.18','0.94','0.72','\Delta
T_\lambda','location','northeast');
grid minor;
set(gca,'XMinorGrid','off','Xgrid','on');
hold off;

%Tau vs. T for different Q
figure(200);
plot(data580(:,1),data580(:,5),'pr','markers',12);
…
set(gca,'XTick', 1.6:0.1:2.2,'YTick',0:0.2:2.2);
axis([1.6 2.2 0 2.2]);
xlabel('\bf Temperature in K');
ylabel('\bf Tau in s');
title('\bf Evaluation Measurement - C1 Sensor');
legend('5.80','4.75','3.66','2.59','1.80','1.18','0.94','location','southeast
');
grid minor;
set(gca,'XMinorGrid','off','Xgrid','on');
hold on;

% %Tau vs. T for different Q (w/ error bars!)
figure(300);
errorbar(data580(:,1),data580(:,5),data580(:,6), '.k','markers',6);
hold on;
…
set(gca,'XTick', 1.6:0.1:2.2,'YTick',0:0.2:2.2);
axis([1.6 2.2 0 2.2]);
xlabel('\bf Temperature in K');
ylabel('\bf Tau in s');
title('\bf Evaluation Measurement - C1 Sensor');
legend('5.80','4.75','3.66','2.59','1.80','1.18','0.94','location','southeast
');
grid on;
set(gca,'XMinorGrid','off','Xgrid','on');
hold off;
```

```
%Tau 1 compared to Tau 2 vs. T for different Q
figure(400);
plot(data580(:,1),data580(:,7),'pr','markers',12);
hold on;
…
axis([1.6 2.2 0 200]);
xlabel('\bf Temperature in K');
ylabel('\bf Tau 1 vs. Tau 2 in %');
title('\bf Evaluation Measurement - C1 Sensor');
legend('5.80','4.75','3.66','2.59','1.80','1.18','0.94','0.72','0.62','locati
on','southeast');
grid minor;
set(gca,'XMinorGrid','off','Xgrid','on');
hold off;

%deltaT vs. Q
figure(500);
plot(dataTemp170(:,2),dataTemp170(:,3),'pr','markers',12);
hold on;
…
axis([0.5 6 0 120]);
xlabel('\bf Heat input in mW/ccm');
ylabel('\bf Temperature rise in mK');
title('\bf Evaluation Measurement - C1 Sensor');
legend('1.70','1.80','1.85','1.90','1.95','2.00','2.05','2.10','location','so
utheast');
grid minor;
set(gca,'XMinorGrid','off','Xgrid','on');
hold off;

%Tau1 vs. Q
figure(600);
plot(dataTemp170(:,2),dataTemp170(:,5),'pr','markers',12);
hold on;
…
axis([0.5 6 0 2]);
xlabel('\bf Heat input in mW/ccm');
ylabel('\bf Tau in s');
title('\bf Evaluation Measurement - C1 Sensor');
grid minor;
set(gca,'XMinorGrid','off','Xgrid','on');
hold off;

%3D plot: Tau vs. T vs. Q
figure(700);
x = data(:,2);
y = data(:,1);
z = data(:,5);
dx = 0.1;
dy = 0.01;
x_edge=[floor(min(x)):dx:ceil(max(x))];
y_edge=[floor(min(y)):dy:ceil(max(y))];
[X,Y]=meshgrid(x_edge,y_edge);
F=TriScatteredInterp(x,y,z);
Z=F(X,Y);
surf(X,Y,Z);
hold on;
axis([0.5 6 1.6 2.2 0.2 1.6]);
xlabel('\bf Heat input in mW/ccm');
ylabel('\bf Temperature in K');
zlabel('\bf Tau in s');
title('\bf Evaluation Measurement - C1 Sensor');
grid minor;
set(gca,'XMinorGrid','off','Xgrid','on');
hold off;

%3D plot: deltaT vs. T vs. Q
figure(800);
x = data(:,2);
y = data(:,1);
z = data(:,3);
dx = 0.1;
dy = 0.01;
x_edge=[floor(min(x)):dx:ceil(max(x))];
y_edge=[floor(min(y)):dy:ceil(max(y))];
[X,Y]=meshgrid(x_edge,y_edge);
F=TriScatteredInterp(x,y,z);
Z=F(X,Y);
surf(X,Y,Z);
hold on;
axis([0.5 6 1.6 2.2 0 110]);
xlabel('\bf Heat input in mW/ccm');
ylabel('\bf Temperature in K');
zlabel('\bf Temperature increase in mK');
title('\bf Evaluation Measurement - C1 Sensor');
grid minor;
set(gca,'XMinorGrid','off','Xgrid','on');
hold off;
```

```
%Single file calculation
files=strcat(folder,singleFilename);
Resistance=str2num(cell2mat(cellfun(@(str) str(29:31), singleFilename,
'UniformOutput', false)));

Heat=1/(-0.59571+0.00489*sqrt(157.09^2+Resistance^2));

timeC1= dlmread(char(files),'\t',[RowStart ColumnTimeC1 RowEnd
ColumnTimeC1]);
temperatureC1= dlmread(char(files),'\t',[RowStart ColumnTempC1 RowEnd
ColumnTempC1]);

timeCbath= dlmread(char(files),'\t',[RowStart ColumnTimeCbath RowEnd
ColumnTimeCbath]);
temperatureCbath = dlmread(char(files),'\t',[RowStart ColumnTempCbath RowEnd
ColumnTempCbath]);

zoneCounter = 1;
zonePoints = 0;
diffTemp = abs(diff(temperatureC1));
tolDiff = 5*mean(diffTemp);
i = 1;
while i < length(temperatureC1);
    if diffTemp(i) > tolDiff;
        zonePoints(zoneCounter) = i;
        zoneCounter = zoneCounter + 1;
    end;
    i = i + 1;
end;

S1C1=mean(temperatureC1(1:zonePoints(1)));

risingExp = zonePoints(zonePoints > 100 & zonePoints < 1000);
fallingExp = zonePoints(zonePoints > 1000);

S3C1=mean(temperatureC1(risingExp(end):fallingExp(1)));
timeC1rel=timeC1(risingExp(1):risingExp(1)+100)-timeC1(risingExp(1));
timeC1S4rel=timeC1(fallingExp(1):fallingExp(1)+100)-timeC1(fallingExp(1));
temperatureC1rel=temperatureC1(risingExp(1):risingExp(1)+100);
temperatureC1S4rel=temperatureC1(fallingExp(1):fallingExp(1)+100);

y = temperatureC1rel;
t = timeC1rel;
x0 = [S3C1,0.5];
F = @(x,xdata)S1C1*exp(-xdata/x(2))+(1-exp(-xdata/x(2)))*x(1);
[x,~,~,~,output]=lsqcurvefit(F,x0,t,y,[],[],opts);

y = temperatureC1S4rel;
t = timeC1S4rel;
x0S4(1) = S1C1;
x0S4(2) = 0.5;
FS4 = @(xS4,xdata)S3C1*exp(-xdata/xS4(2))+(1-exp(-xdata/xS4(2)))*xS4(1);
[xS4,~,~,~,output]=lsqcurvefit(FS4,x0S4,t,y,[],[],opts);

Results2(:,1)=Heat;
Results2(:,2)=S1C1;
Results2(:,3)=(S3C1-S1C1)*1000;

S1C1plot(1:risingExp(1))=S1C1;
S1C1plot=S1C1plot';

for k=1:length(temperatureC1rel);
    S2C1otherplot(k)=S1C1*exp(-timeC1rel(k)/x(2))+(1-exp(-
timeC1rel(k)/x(2)))*x(1);
end;

for k=1:length(temperatureC1S4rel);
    S2C1plot(k)=S3C1*exp(-timeC1S4rel(k)/xS4(2))+(1-exp(-
timeC1S4rel(k)/xS4(2)))*xS4(1);
end;

S2C1plot=S2C1plot';
S3C1plot(1:fallingExp(1)-risingExp(end)+1)=S3C1;
S3C1plot=S3C1plot';

figure(1000);
plot(timeC1,temperatureC1-S1C1,'.b','markers',5);
hold on;
plot(timeC1(1:risingExp(1)),S1C1plot-S1C1,'-r','linewidth',2);
hold on;
plot(timeC1(fallingExp(1):fallingExp(1)+100),S2C1plot-
S1C1,'g','linewidth',2);
hold on;
plot(timeC1(risingExp(end):fallingExp(1)),S3C1plot-S1C1,'-r','linewidth',2);
hold on;
plot(timeC1(risingExp(1):risingExp(1)+100), S2C1otherplot-S1C1, 'g',
'linewidth', 2);
hold on;

% Points above Tlambda

  for x = 1:10
      disp(x)
  end
```

```
% Averaging data

data062av=Averaging(data062);
data072av=Averaging(data072);
data094av=Averaging(data094);
data118av=Averaging(data118);
data180av=Averaging(data180);
data259av=Averaging(data259);
data366av=Averaging(data366);
data475av=Averaging(data475);
data580av=Averaging(data580);

figure(1100);
plot(data580av(:,1),data580av(:,3),'pr','markers',12);
hold on;
…
plot(Tsampling,deltaTlambda,'-.k');
set(gca,'XTick', 1.6:0.1:2.2,'YTick',0:10:110);
axis([1.6 2.2 0 110]);
xlabel('\bf Temperature in K');
ylabel('\bf Temperature rise in mK');
title('\bf Evaluation Measurement - C1 Sensor - Averaged');
legend('5.80','4.75','3.66','2.59','1.80','1.18','0.94','0.72','\Delta
T_\lambda','location','northeast');
grid minor;
set(gca,'XMinorGrid','off','Xgrid','on');
hold off;

figure(1200);
plot(data580av(:,1),data580av(:,5),'pr','markers',12);
hold on;
…
set(gca,'XTick', 0:0.2:2.2);
set(gca,'XTick', 1.6:0.1:2.2,'YTick',0:0.2:2.2);
axis([1.6 2.2 0 2.2]);
xlabel('\bf Temperature in K');
ylabel('\bf Tau in s');
title('\bf Evaluation Measurement - C1 Sensor - Averaged');
legend('5.80','4.75','3.66','2.59','1.80','1.18','0.94','0.72','location','so
utheast');
grid minor;
set(gca,'XMinorGrid','off','Xgrid','on');
hold off;
```

Averaging.m

```
function [data1av] = Averaging(data1)
for m=1:length(data1);
   if m==1;
       counter(1)=1;
       count=1;
   else
       if data1(m,2)==data1(m-1,2);
            counter(count)=counter(count)+1;
       else
            count=count+1;
            counter(count)=1;
       end
   end
end

for m=1:length(counter);
   if m==1;
       istart=1;
   else
       istart=istop;
   end
   istop=istart+counter(m);
   sum=zeros(1,6);
   for k=istart:istop-1;
       sum=sum+data1(k,:);
   end
   data1av(m,:)=sum/(istop-istart);
end
end
```

Matlab script for the temperature sensor calibration

```
% clear;
% clc;
% close all;
format long;
%%
%To do: - provide the csv-files for the calibration in the same folder as
%         this matlab file.
%       -change the variable name "folder" to the chosen directory
%       -Change the diadem script with:
%  1.    ZLC1 ZUC1 and FitCoeffC1Chebychev
%  2.    ZLCbath ZUCbath and FitCoeffCbathCHebychev

folder='C:\Users\jschunde\01WorkJS\AnalysisThesis\2016-10-10-
75MPaUnified\Calibration\C1CbathCalib\';
%filename=cellstr('');
filename=dir('*.csv');
filename = {filename.name };
filename=filename';
Pressure=cellfun(@(str) str(19:22), filename, 'UniformOutput', false);
filename(:,2)=Pressure;
filename=sortrows(filename,-2);
filename(:,2)=[];



numberOfFiles=size(filename,1);
RowStart=1;
RowEnd=100;
ColumnMKSsignal=0;
ColumnVoltageC1=8;
ColumnVoltageCbath=10;

Current=3*10^-6;

A0to9=[1.392408;0.527153;0.166756;0.050988;0.026514;0.001975;-
0.017976;0.005409;0.013259;0];
B=5.6;
C=2.9;

% ZLC1=3.6470627209837;
% ZUC1=3.8315153201152;
% ZLCbath=3.8931701072634;
% ZUCbath=4.1007338409234;

for n=1:numberOfFiles;
    files(n,1)=strcat(folder,filename(n,1));
    ResC1(n,1)=(mean(dlmread(char(files(n,1)),'\t',[RowStart ColumnVoltageC1
RowEnd ColumnVoltageC1])))/Current;
    ZC1(n,1)=log10(ResC1(n,1));
    ResCbath(n,1)=(mean(dlmread(char(files(n,1)),'\t',[RowStart
ColumnVoltageCbath RowEnd ColumnVoltageCbath])))/Current;
    ZCbath(n,1)=log10(ResCbath(n,1));
end
ZLC1=ZC1(1)-0.001;
ZUC1=ZC1(end)+0.001;
ZLCbath=ZCbath(1)-0.001;
ZUCbath=ZCbath(end)+0.001;

for n=1:numberOfFiles;
files(n,1)=strcat(folder,filename(n,1));

MKSpressure(n,1)=1000*(mean(dlmread(char(files(n,1)),'\t',[RowStart
ColumnMKSsignal RowEnd ColumnMKSsignal])));
TemperatureITS90(n,1)=A0to9(1)...
+(A0to9(2)*((log(MKSpressure(n))-B)/C)^1)...
+(A0to9(3)*((log(MKSpressure(n))-B)/C)^2)...
+(A0to9(4)*((log(MKSpressure(n))-B)/C)^3)...
+(A0to9(5)*((log(MKSpressure(n))-B)/C)^4)...
+(A0to9(6)*((log(MKSpressure(n))-B)/C)^5)...
+(A0to9(7)*((log(MKSpressure(n))-B)/C)^6)...
+(A0to9(8)*((log(MKSpressure(n))-B)/C)^7)...
+(A0to9(9)*((log(MKSpressure(n))-B)/C)^8)...
+(A0to9(10)*((log(MKSpressure(n))-B)/C)^9);

% ResC1(n,1)=(mean(dlmread(char(files(n,1)),'\t',[RowStart ColumnVoltageC1
RowEnd ColumnVoltageC1])))/Current;
% ZC1(n,1)=log10(ResC1(n,1));
kC1(n,1)=((ZC1(n,1)-ZLC1)-(ZUC1-ZC1(n,1)))/(ZUC1-ZLC1);

%ResCbath(n,1)=(mean(dlmread(char(files(n,1)),'\t',[RowStart
ColumnVoltageCbath RowEnd ColumnVoltageCbath])))/Current;
% ZCbath(n,1)=log10(ResCbath(n,1));
kCbath(n,1)=((ZCbath(n,1)-ZLCbath)-(ZUCbath-ZCbath(n,1)))/(ZUCbath-ZLCbath);
end

foChebychev = fitoptions('Method','NonLinearLeastSquares',...
               'Algorithm','Trust-Region',...
               'Lower',[-10,-10,-10,-10,-10,-10,-10,-10,-10],...
%lower bounds
               'Upper',[10,10,10,10,10,10,10,10,10],...
%upper bounds
               'StartPoint',[5.465897,-6.310096,2.863560,-1.089653,0.350715,-
0.091305,0.016109,0.000115,-0.002003],...
               'DiffMaxChange',10e-12,...
               'DiffMinChange',10e-12,...
               'MaxFunEvals',10000,...
               'MaxIter',5000);
```

```
ftChebychev =
fittype('a*cos(0*acos(x))+b*cos(1*acos(x))+c*cos(2*acos(x))+d*cos(3*acos(x))+
e*cos(4*acos(x))+f*cos(5*acos(x
))+g*cos(6*acos(x))+h*cos(7*acos(x))+hh*cos(8*acos(x))','options',foChebychev
);

[fC1Chebychev,gofC1Chebychev] =
fit(kC1,TemperatureITS90,ftChebychev,foChebychev);
FitCoeffC1Chebychev=coeffvalues(fC1Chebychev);

figure(100);
plot(fC1Chebychev,kC1,TemperatureITS90,'fit','residuals');
legend Location SouthWest;
xlabel('\bf kCernox1');
ylabel('\bf deviation in K');
subplot(2,1,1);
title('\bf Fitting Cernox 1 Chebychev');
legend Location NorthWest;
xlabel('\bf kCernox1');
ylabel('\bf Temperature in K');

[fCbathChebchev,gofCbathChebychev] =
fit(kCbath,TemperatureITS90,ftChebychev,foChebychev);
FitCoeffCbathChebychev=coeffvalues(fCbathChebchev);
figure(200);
plot(fCbathChebchev,kCbath,TemperatureITS90,'fit','residuals');
xlabel('\bf kCernoxBath');
ylabel('\bf deviation in K');
legend Location SouthWest;
subplot(2,1,1);
title('\bf Fitting Cernox Bath Chebychev');
legend Location NorthWest;
xlabel('\bf kCernoxBath');
ylabel('\bf Temperature in K');

for o=1:numberOfFiles;
TC1Chebychev(o,1)=FitCoeffC1Chebychev(1)*cos(0*acos(kC1(o)))+FitCoeffC1Chebyc
hev(2)*cos(1*acos(kC1(o)))+FitCoeffC1Chebychev(3)*cos(2*acos(kC1(o)))+FitCoef
fC1Chebychev(4)*cos(3*acos(kC1(o)))+FitCoeffC1Chebychev(5)*cos(4*acos(kC1(o))
)+FitCoeffC1Chebychev(6)*cos(5*acos(kC1(o)
))+FitCoeffC1Chebychev(7)*cos(6*acos(kC1(o)))+FitCoeffC1Chebychev(8)*cos(7*ac
os(kC1(o)))+FitCoeffC1Chebychev(9)*cos(8*acos(kC1(o)));
TCbathChebychev(o,1)=FitCoeffCbathChebychev(1)*cos(0*acos(kCbath(o)))+FitCoef
fCbathChebychev(2)*cos(1*acos(kCbath(o)))+FitCoeffCbathChebychev(3)*cos(2*aco
s(kCbath(o)))+FitCoeffCbathChebychev(4)*cos(3*acos(kCbath(o)))+FitCoeffCbathC
hebychev(5)*cos(4*acos(kCbath(o)))+FitCoeffCbathChebychev(6)*cos(5*acos(kCbat
h(o)
))+FitCoeffCbathChebychev(7)*cos(6*acos(kCbath(o)))+FitCoeffCbathChebychev(8)
*cos(7*acos(kCbath(o)))+FitCoeffCbathChebychev(9)*cos(8*acos(kCbath(o)));
end
Cernox1=[MKSpressure,ResC1];
```

```
foExponential = fitoptions('Method','NonLinearLeastSquares',...
               'Algorithm','Trust-Region',...
               'Lower',[-10e8,-10e8,-10e8,-10e8],...
%lower bounds
               'Upper',[10e8,10e8,10e8,10e8],...
%upper bounds
               'StartPoint',[969015,-1.75961,68.4698,-0.433457],...
               'DiffMaxChange',10e-12,...
               'DiffMinChange',10e-12,...
               'MaxFunEvals',10000,...
               'MaxIter',5000);

ftExponential = fittype('aa*exp(bb*log(x))
+cc*exp(dd*log(x))','options',foExponential);

[fC1Exponential,gofC1Exponential] =
fit(ResC1,TemperatureITS90,ftExponential,foExponential);
FitCoeffC1Exponential=coeffvalues(fC1Exponential);
figure(300);
plot(fC1Exponential,ResC1,TemperatureITS90,'fit','residuals');
legend Location SouthWest;
xlabel('\bf Resistance C1 in Ohm');
ylabel('\bf deviation in K');
subplot(2,1,1);
title('\bf Fitting Cernox 1 Exponential');
legend Location NorthWest;
xlabel('\bf Resistance Cbath in Ohm');
ylabel('\bf Temperature in K');

[fCbathExponential,gofCbathExponential] =
fit(ResCbath,TemperatureITS90,ftExponential,foExponential);
FitCoeffCbathExponential=coeffvalues(fCbathExponential);
figure(400);
plot(fCbathExponential,ResCbath,TemperatureITS90,'fit','residuals');
xlabel('\bf Resistance Cbath in Ohm');
ylabel('\bf deviation in K');
legend Location SouthWest;
subplot(2,1,1);
title('\bf Fitting Cernox Bath Exponential');
legend Location NorthWest;
xlabel('\bf Resistance Cbath in Ohm');
ylabel('\bf Temperature in K');
```

VB script to convert the *.tdms-files in *.csv-files

```
'-------------------------------------------------------------------------------
'-- VBS script file
'-- Created on 15.10.2016 20:30
'-- Author: Jens Schundelmeier
'-- Comment: Analysis Script for Measurements with Cernox1 and Cernox Bath in HeII
'-------------------------------------------------------------------------------

Option Explicit  'Forces the explicit declaration of all the variables in a script.
'ZL and ZU Cernox 1
R1=3.64682537545811
R2=3.83131609708584

'Fit CoeffC1
R3=1.90790146067763
R4=-0.248104534767726
R5=0.0127117214757209
R6=-0.00112096468356139
R7=0.000398575327960991
R8=-4.71081524917510e-05
R9=-0.000151551589812306
R10=0.000177766800384339
R11=-3.40789807418508e-06


'ZL and ZU Cernox Bath
R12=3.89299640870702
R13=4.10054868522582

'Fit CoeffCbath
R14=1.90786726401622
R15=-0.247846501065370
R16=0.0125355944674792
R17=-0.00120535413528483
R18=0.000709792267010703
R19=-0.000252265491024423
R20=9.83027458974787e-06
R21=0.000118724834551761
R22=-0.000187863694843698

'Change Pathvariable!!!
Dim vFoundFiles, iCount, file, PATHVARIABLE
PATHVARIABLE="C:\Users\jschunde\01WorkJS\AnalysisThesis\2016-10-10-
75MPaUnified\C1Cbath" & "\"

vFoundFiles = DirListGet(PATHVARIABLE, "*.tdms", "filename", "FullFilenames")
If IsArray(vFoundFiles) Then
  For iCount = Lbound(vFoundFiles) to Ubound(vFoundFiles)
    file = vFoundFiles(iCount)
    Call DataFileLoad(file, "TDMS", "Load")

    Call Data.Root.ChannelGroups.Add("Data Analysis", 3).Activate()

    'Trigger
    Call Calculate("Ch(""[3]/TimeRelTrigger"") = Ch(""[2]/Timestamp Trigger"")-
ChnPropGet(""[2]/Timestamp Trigger"", ""minimum"")",NULL,NULL,"")
    Call ChnClpCopy("[2]/Trigger")
    Call ChnClpPaste(12)
    Call
Data.Move(Data.Root.ChannelGroups(3).Channels("Trigger"),Data.Root.ChannelGroups(3).Ch
annels,2)

    'Calculate MKS Temperature
    Call ChnFromWfXGen("[1]/MKS Pressure","[3]/TimeRelMKSBath","WfXRelative")
    Data.Root.ChannelGroups(3).Channels("NoName").Name = "TimeRelMKSBath"
    Call Calculate("Ch(""[3]/PaMKSBath"") = 1000*Ch(""[1]/MKS
Pressure"")",NULL,NULL,"")
    Call Calculate("Ch(""[3]/TempAbsMKSBath"") = 1.392408 +
0.527153*((log(Ch(""[3]/PaMKSBath""))-5.6)/2.9)^1 +
0.166756*((log(Ch(""[3]/PaMKSBath""))-5.6)/2.9)^2 +
0.050988*((log(Ch(""[3]/PaMKSBath""))-5.6)/2.9)^3 +
0.026514*((log(Ch(""[3]/PaMKSBath""))-5.6)/2.9)^4 +
0.001975*((log(Ch(""[3]/PaMKSBath""))-5.6)/2.9)^5 -
0.017976*((log(Ch(""[3]/PaMKSBath""))-5.6)/2.9)^6 +
0.005409*((log(Ch(""[3]/PaMKSBath""))-5.6)/2.9)^7 +
0.013259*((log(Ch(""[3]/PaMKSBath""))-5.6)/2.9)^8 ",NULL,NULL,"")
    Call ChnOffset("[3]/TempAbsMKSBath","/TempRelMKSBath",50,"mean value offset")

    'Calculate Cernox 1 Temperature

    Call Calculate("Ch(""[3]/TimeRelCernox1Sample"") = Ch(""[2]/Timestamp Cernox1
Sample"")-ChnPropGet(""[2]/Timestamp Trigger"", ""minimum"")",NULL,NULL,"")
    Call Calculate("Ch(""[3]/ResCernox1Sample"") = abs(Ch(""[2]/Cernox1 Sample"") /
(3e-6))",NULL,NULL,"")
    Call Calculate("Ch(""[3]/kCernox1Sample"") = ((lg(Ch(""[3]/ResCernox1Sample""))-
R1 )-( R2 -lg(Ch(""[3]/ResCernox1Sample""))))/( R2 - R1 )",NULL,Null,"")
    Call Calculate("Ch(""[3]/TempAbsCernox1Sample"")=  R3
*cos(0*acos(Ch(""[3]/kCernox1Sample"") ))+ R4 *cos(1*acos(Ch(""[3]/kCernox1Sample"")
))+ R5 *cos(2*acos(Ch(""[3]/kCernox1Sample"") ))+ R6
*cos(3*acos(Ch(""[3]/kCernox1Sample"") ))+ R7 *cos(4*acos(Ch(""[3]/kCernox1Sample"")
))+ R8 *cos(5*acos(Ch(""[3]/kCernox1Sample"") ))+ R9
*cos(6*acos(Ch(""[3]/kCernox1Sample"") ))+ R10 *cos(7*acos(Ch(""[3]/kCernox1Sample"")
))+ R11 *cos(8*acos(Ch(""[3]/kCernox1Sample"") ))",NULL,NULL,"")
    Call ChnOffset("[3]/TempAbsCernox1Sample","/TempRelCernox1Sample",50,"mean value
offset")

    'Calculate Cernox bath Temperature
    Call Calculate("Ch(""[3]/TimeRelCernoxBath"") = Ch(""[2]/Timestamp Cernox Bath"")-
ChnPropGet(""[2]/Timestamp Trigger"", ""minimum"")",NULL,NULL,"")
    Call Calculate("Ch(""[3]/ResCernoxBath"") = abs(Ch(""[2]/Cernox Bath"") / (3e-
6))",NULL,NULL,"")
    Call Calculate("Ch(""[3]/kCernoxBath"") = ((lg(Ch(""[3]/ResCernoxBath""))- R12 )-(
R13 -lg(Ch(""[3]/ResCernoxBath""))))/( R13 - R12)",NULL,Null,"")
    Call Calculate("Ch(""[3]/TempAbsCernoxBath"") = R14
*cos(0*acos(Ch(""[3]/kCernoxBath"") ))+ R15 *cos(1*acos(Ch(""[3]/kCernoxBath"") ))+
R16 *cos(2*acos(Ch(""[3]/kCernoxBath"") ))+ R17 *cos(3*acos(Ch(""[3]/kCernoxBath"")
))+ R18 *cos(4*acos(Ch(""[3]/kCernoxBath"") ))+ R19
*cos(5*acos(Ch(""[3]/kCernoxBath"") ))+ R20 *cos(6*acos(Ch(""[3]/kCernoxBath"") ))+
R21 *cos(7*acos(Ch(""[3]/kCernoxBath"") ))+ R22 *cos(8*acos(Ch(""[3]/kCernoxBath"")
))",NULL,NULL,"")
    Call ChnOffset("[3]/TempAbsCernoxBath","/TempRelCernoxBath",50,"mean value
offset")

    Dim oMyChannelList
    Set oMyChannelList = Data.GetChannels("[1]/Channel*")
    Call oMyChannelList.Add(Data.Root.ChannelGroups(3))
    Call DataFileSaveSel(PATHVARIABLE & DataSetName & ".csv", "CSV", oMyChannelList)


    Call DataDelAll()
  Next
End If
```

```
'-------------------------------------------------------------------------------
'-- VBS script file
'-- Created on 15.10.2016 20:30
'-- Author: Jens Schundelmeier
'-- Comment: Analysis Script for Measurements with Cernox1 and Cernox Bath in HeII
'-------------------------------------------------------------------------------

Option Explicit  'Forces the explicit declaration of all the variables in a script.
'ZL and ZU Cernox 1
R1=969015
R2=-1.75888191356891
R3=67.6750963530335
R4=-0.432189457377721

'Fit CoeffCbath
R5=969015
R6=-1.66213379339641
R7=63.9959001606878
R8=-0.395853134410943

'Change Pathvariable!!!
Dim vFoundFiles, iCount, file, PATHVARIABLE
PATHVARIABLE="C:\Users\jschunde\01WorkJS\AnalysisThesis\2016-10-10-
75MPaUnified\C1Cbath" & "\"


vFoundFiles = DirListGet(PATHVARIABLE, "*.tdms", "filename", "FullFilenames")
If IsArray(vFoundFiles) Then
  For iCount = Lbound(vFoundFiles) to Ubound(vFoundFiles)
    file = vFoundFiles(iCount)
    Call DataFileLoad(file, "TDMS", "Load")

    Call Data.Root.ChannelGroups.Add("Data Analysis", 3).Activate()

    'Trigger
    Call Calculate("Ch(""[3]/TimeRelTrigger"") = Ch(""[2]/Timestamp Trigger"")-
ChnPropGet(""[2]/Timestamp Trigger"", ""minimum"")",NULL,NULL,"")
    Call ChnClpCopy("[2]/Trigger")
    Call ChnClpPaste(12)
    Call
Data.Move(Data.Root.ChannelGroups(3).Channels("Trigger"),Data.Root.ChannelGroups(3).Ch
annels,2)

    'Calculate MKS Temperature
    Call ChnFromWfXGen("[1]/MKS Pressure","[3]/TimeRelMKSBath","WfXRelative")
    Data.Root.ChannelGroups(3).Channels("NoName").Name = "TimeRelMKSBath"
    Call Calculate("Ch(""[3]/PaMKSBath"") = 1000*Ch(""[1]/MKS
Pressure"")",NULL,NULL,"")
    Call Calculate("Ch(""[3]/TempAbsMKSBath"") = 1.392408 +
0.527153*((log(Ch(""[3]/PaMKSBath""))-5.6)/2.9)^1 +
0.166756*((log(Ch(""[3]/PaMKSBath""))-5.6)/2.9)^2 +
0.050988*((log(Ch(""[3]/PaMKSBath""))-5.6)/2.9)^3 +
0.026514*((log(Ch(""[3]/PaMKSBath""))-5.6)/2.9)^4 +
0.001975*((log(Ch(""[3]/PaMKSBath""))-5.6)/2.9)^5 -
0.017976*((log(Ch(""[3]/PaMKSBath""))-5.6)/2.9)^6 +
0.005409*((log(Ch(""[3]/PaMKSBath""))-5.6)/2.9)^7 +
0.013259*((log(Ch(""[3]/PaMKSBath""))-5.6)/2.9)^8 ",NULL,NULL,"")
    Call ChnOffset("[3]/TempAbsMKSBath","/TempRelMKSBath",50,"mean value offset")

    'Calculate Cernox 1 Temperature

    Call Calculate("Ch(""[3]/TimeRelCernox1Sample"") = Ch(""[2]/Timestamp Cernox1
Sample"")-ChnPropGet(""[2]/Timestamp Trigger"", ""minimum"")",NULL,NULL,"")
    Call Calculate("Ch(""[3]/ResCernox1Sample"") = abs(Ch(""[2]/Cernox1 Sample"") /
(3e-6))",NULL,NULL,"")
    Call Calculate("Ch(""[3]/kCernox1Sample"") =
Ch(""[3]/ResCernox1Sample"")",NULL,Null,"")
    Call Calculate("Ch(""[3]/TempAbsCernox1Sample"")=
R1*exp(R2*ln(Ch(""[3]/ResCernox1Sample"")))
+R3*exp(R4*ln(Ch(""[3]/ResCernox1Sample"")))",NULL,NULL,"")
    Call ChnOffset("[3]/TempAbsCernox1Sample","/TempRelCernox1Sample",50,"mean value
offset")

    'Calculate Cernox bath Temperature

    Call Calculate("Ch(""[3]/TimeRelCernoxBath"") = Ch(""[2]/Timestamp Cernox Bath"")-
ChnPropGet(""[2]/Timestamp Trigger"", ""minimum"")",NULL,NULL,"")
    Call Calculate("Ch(""[3]/ResCernoxBath"") = abs(Ch(""[2]/Cernox Bath"") / (3e-
6))",NULL,NULL,"")
    Call Calculate("Ch(""[3]/kCernoxBath"") = Ch(""[3]/ResCernoxBath"")",NULL,Null,"")
    Call Calculate("Ch(""[3]/TempAbsCernoxBath"") =
R5*exp(R6*ln(Ch(""[3]/ResCernoxBath"")))
+R7*exp(R8*ln(Ch(""[3]/ResCernoxBath"")))",NULL,NULL,"")
    Call ChnOffset("[3]/TempAbsCernoxBath","/TempRelCernoxBath",50,"mean value
offset")

    Dim oMyChannelList
    Set oMyChannelList = Data.GetChannels("[1]/Channel*")
    Call oMyChannelList.Add(Data.Root.ChannelGroups(3))
    Call DataFileSaveSel(PATHVARIABLE & DataSetName & ".csv", "CSV", oMyChannelList)


    Call DataDelAll()
  Next
End If
```